AD 729948

ROCK MECHANICS & EXPLOSIVES RESEARCH CENTER

UNIVERSITY OF MISSOURI - ROLLA

PENETRATION IN GRANITE BY SHAPED CHARGE LINERS
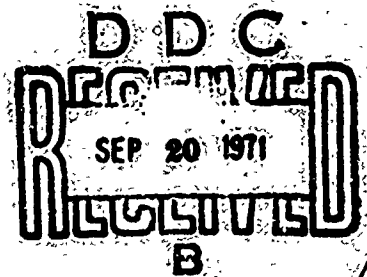
OF VARIOUS METALS

Approved for Public release; distribution unlimited

Final Report for

DuPont DeNemours Co., Inc.
Wilmington, Delaware

and

Corps of Engineers
Missouri River Division
Omaha, Nebraska

Contract No. DACA-45-69-C-0087

April 1971

D D C
RECEIVED
1971
A

D D C
RECEIVED
SEP 20 1971
B

ROCK MECHANICS & EXPLOSIVES RESEARCH CENTER

UNIVERSITY OF MISSOURI - ROLLA

**Details of illustrations in
this document may be better
studied on microfiche**

PENETRATION IN GRANITE BY SHAPED CHARGE LINERS

OF VARIOUS METALS

by

R.R. Rollins, Assoc. Prof. of Min. Eng.,
& Sr. Invest. in RMERC;
G.B. Clark, Prof. of Min. Eng.,
& Director, RMERC;
H.N. Kalia, Grad. Res. Asst., RMERC

Approved for public release; distribution unlimited

Final Report for

DuPont De Nemours Co., Inc.
Wilmington, Delaware

and

Corps of Engineers
Missouri River Division
Omaha, Nebraska

Contract No. DACA-45-69-C-0087

April 1971

I. INTRODUCTION

A. General

The term "shaped charges" is generally applied to high explosive cylindrical charges with lined or unlined cavities formed at the end opposite to the point of initiation. The unlined cavity effect is known as the Munroe effect in the United States and the United Kingdom (1), the Neumann effect in Germany, and the cumulation effect in Russia (2). There is no evidence that Munroe or Neumann discovered the lined-cavity effect, which is a phenomenon quite different from the unlined-cavity effect. Baum (2) has credited Sukhreski with the systematic investigation of the cumulation effect. Eichelberger (3) credits R.W. Wood with the recognition in 1936 of the usefulness of metallic liners in the hollowed charges to produce fragments of extremely high velocity. Fundamental and developmental studies as well as the design of shaped charge weapons were simultaneously undertaken by DuPont's Eastern Laboratories, and by Kistiakowsky, Taylor, MacDougal, Jacobs, and others in 1941.

This study was undertaken to determine the penetrability of shaped charge jets into granite utilizing metallic liners and composition C-4 as the high explosive. While shaped charges have found extensive use in military applications, industrial uses are limited to oil well casing perforations, furnace tapping, and linear metal cutting charges.

Lined cavity charges were investigated by Clark (4), Austin (5), and Huttl (6), to evaluate their effect in breaking concrete, rhyolite, and limestone boulders. From the literature it appears that no systematic investigation has been made to evaluate shaped charges for drilling and blasting rock. The capability of relatively inexpensive shaped charges to form high velocity jets makes them of interest for possible application in this operation.

B. Nature of the Investigation.

The primary objective of this study was to evaluate the penetrating capability into rocks of shaped charges fabricated from selected liner metals. The following parameters were investigated: 1) property effects of six different liner metals, 2) change in the physical

properties of liners by annealing, 3) behavior of rock under jet impact, and 4) jet characteristics, formation, and penetration theory.

A large amount of information is available on the penetration of metallic targets by metallic jets. The first order penetration law was developed independently by Pack, Mott, and Hill (7), Pugh (1), and Pack and Evans (8, 9) applying Bernoulli's theorem. The total penetration is given by:

$$P = L \ (\rho_j/\rho_t)^{\frac{1}{2}} \tag{1)*}$$

Equation (1) holds only for ideal jets and for targets with zero yield strength as compared to the pressure of the jet. Thus, one expects variation from this law for nine ideal materials. It is observed that the resistance to penetration in rock is due not only to the density of the jet and its length and the density of the rock, but to other factors as well, e.g., the joints, bedding planes, porosity, and the anisotropic nature of the target.

II. THEORY OF JET FORMATION AND PENETRATION

The classical two-dimensional theory of jet formation (8, 10) has been modified (3) to account for the jet tip velocity gradient. The modified two-dimensional theory visualizes the liner collapsing upon itself due to the pressure of the detonation products. As the pressure is applied progressively to the liner, it collapses upon the axis at an angle α (Figure 1). This collapse angle is greater than the apex angle of the cone.

The two-dimensional theory and other similar theories neglect the acceleration of the coordinate of the stagnation point and the thickening of the liner. In order to account for these parameters one requires the solution of a three-dimensional time dependent configuration.

A. <u>Theory of Cone Collapse and Jet Formation</u>. The analytical technique used for collapsing cylindrical shells (11) may be applied to collapsing

---

* List of symbols - Appendix A

2

conical liners. According to this theory, when an undisturbed cylindrical shell contracts the velocity of the outher surface would tend to diminish and the inner velocity should increase (Figure 1). As an initial approximation, it is assumed that the liner material is incompressible and that the wall moves inward normal to the original surface of the cone.

For a cone of half apex angle α (Figure 2) the kinetic energy of a thin element of unit thickness can be obtained by considering the section to collapse along the slant height of the cone AB. The kinetic energy of this element is

$$T = \rho\pi\cos\alpha(S_3\dot{S_3})^2 \ln S_2/S_3 \tag{2}$$

or the time of collapse is given by

$$t_c = (\rho\pi\Delta l \cos\alpha/T)^{\frac{1}{2}} \; 1/2 \int_{r_j/\cos\alpha}^{S_{3i}} S_3 \ln\left(\frac{S_3 + d}{S_3}\right) dS_3 \tag{3}$$

Equation (3) may be numerically integrated for successive values of S_{3i} and the time of collapse determined for a constant collapse velocity. For a constant jet radius the movement of the stagnation point is constant (Fig. 3). This partially explains why the two-dimensional theory offers such a good approximation for a three-dimensional process. Modifications similar to those employed by Eichelberger (12) and Jackson (13) will yield more accurate evaluation of jet formation and of the physical processes involved.

B. Theory of Jet Penetration. The basic theory of penetration by high-speed metallic jets was developed using Bernoulii's theorem (Equation 1). Various authors have modified this equation with empirical constants to explain penetration of various types of metallic targets; however, it does not take into account the jet velocity and target strength. Dipersio (14) has modified the equations developed by Allison and Vitali (15), and the concept of his theory (14) treats three cases: (a) a continuous jet, (b) a partially continuous jet, and (c) a completely discontinuous jet. The total penetration for these three conditions is given by

$$P_T = Z_o \left[V_j^o/(1 + \gamma)u^{min} \right]^{1/\gamma} -1 \tag{4}$$

3

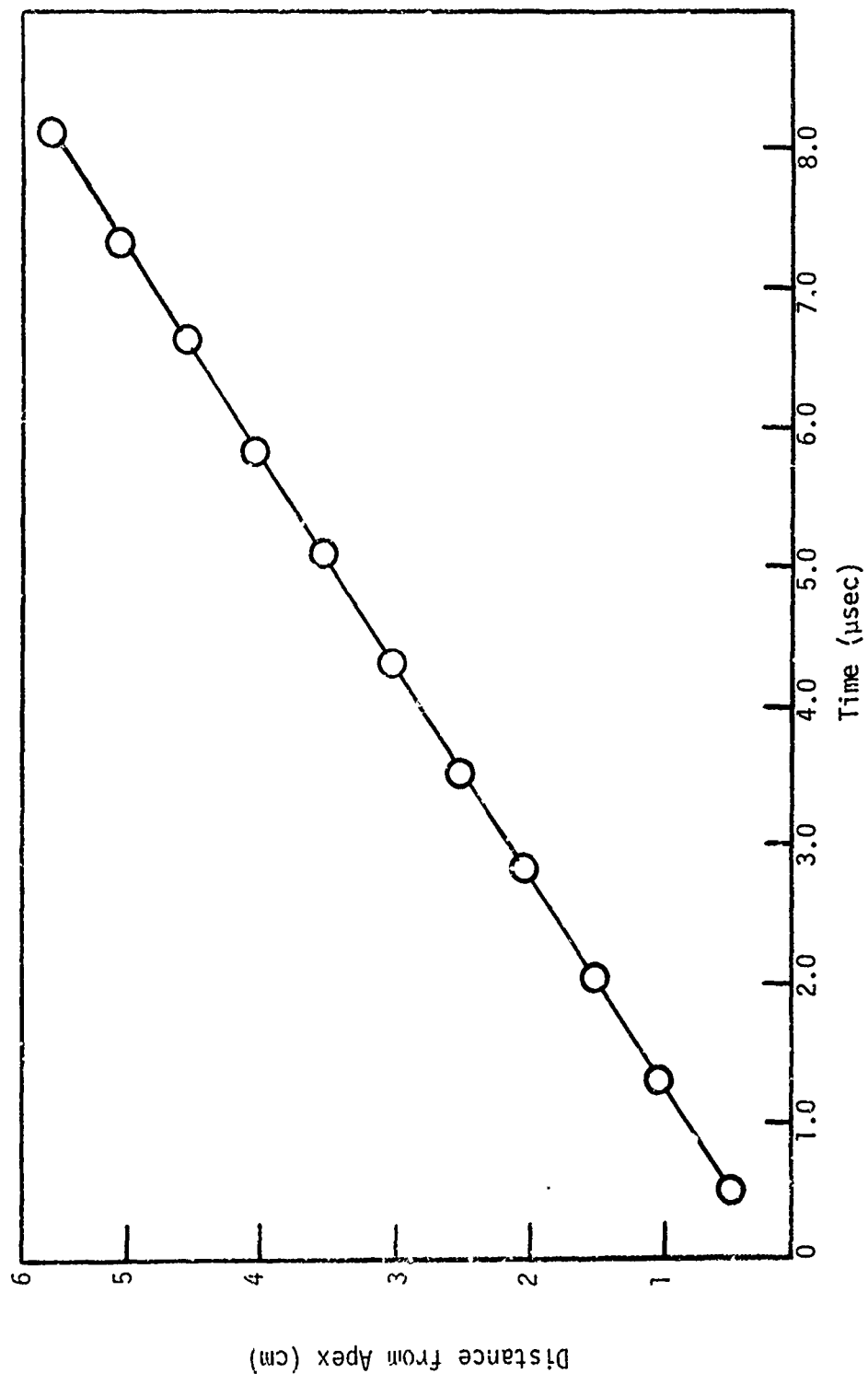Figure 1. Cone Collapse and Jet Formation

Figure 2. Cone Collapse Dimensions

4

Figure 3. Collapse Time for 60 Degree Liners

$$P_T = \frac{(1 + \gamma)(V_j^0 t_1)^{1/(1+\gamma)} Z_0^{\gamma/(1+\gamma)}}{\gamma}$$

$$\qquad\qquad (5)$$

$$- \frac{\sqrt{(1 + \gamma)U^{min} t_1 (V_j^0 t_1)^{1/(1+\gamma)} Z_0^{\gamma/(1+\gamma)}}}{\gamma} - Z_0$$

$$P_T = \frac{V_j^0 t_1 - \sqrt{U^{min} t_1 (V_j^0 t_1 + \gamma Z_0)}}{\gamma}$$

$$\qquad\qquad (6)$$

The basic assumptions in the development of equations (4), (5), and (6) are that the target and jet are incompressible, the jet originates at a distance Z_0 from the target, the jet breaks up axially into individual particles simultaneously throughout its entire length, and all particles above a critical velocity for a particular target contribute to penetration.

For a given charge and target the penetration increases linearly with Z_0 for a continuous jet (equation 4). The penetration increases with jet tip velocity and with a decrease in U^{min}, the minimum penetration velocity, both of which can be determined experimentally. The jet tip velocity is a function of liner and explosive properties.

Maximum penetration is obtained at the upper limit of application of equation (6), which defines the penetration for a partially continuous jet. The maximum penetration is given by

$$P_{max} = \sqrt{\frac{\rho_j}{\rho_t}} \left[V_j^0 - \sqrt{U^{min} \left(V_j^0 + \gamma \frac{Z_0}{t_1} \right)} \right]$$

$$\qquad\qquad (7)$$

Maximum penetration is obtained for high jet tip velocity and optimum jet breakup time, t_1. This equation offers an explanation of the reason that high velocity explosives and high density cohesive jets produce a maximum target penetration.

6

III. EXPERIMENTAL DESIGN

A. Design of Shaped Charges. A concise summary of shaped charge design is given by Klamer (16). For this investigation the following design parameters were considered:

(1) liner material, (2) apex angle, (3) liner thickness, (4) charge dimensions, (5) type of explosive, and (6) target material.

1. Liner material. Zernow (17) tested several metals for shaped charge liners and arrived at the conclusion that copper, nickel, aluminum, and silver (all face centered cubic) behave in a similar manner with few noticeable differences between them. They respond in a ductile fashion in the dynamic Bridgman region, and stretch in a taffy-like manner in the jet flight phase. Copper is the most effective liner material for metal targets because of its ductility, cost and density.

Iron (body centered cubic) and all 1020 mild steels showed high ductility in the dynamic Bridgman region but fractured in relatively large fragments shortly after leaving the high pressure region. The hexagonal metals tested by Zernow (17) show distinct characteristics. In the flight phase the jets from these metals break up into fine fragments. Magnesium shows a ductile nature in the dynamic Bridgman region while cobalt exhibits an anomalous behavior.

Metals under higher pressures (21,000-31,500 kg/cm^2) show a different degree of elongation than they do under ambient pressures. The amount of energy imparted to plastic flow and fracturing changes as pressure is increased (18), hence the mode of liner failure will change with the applied pressure. Metals having low melting points, cadmium (hexagonal), zinc (hexagonal), lead (face centered), and tin (tetragonal), all behave in a unique manner despite the diversity in their crystal structure. It appears that for those having melting points $\geq 625°C$ the crystal structure correlates with the observed behavior of the jet, whereas in low melting point metals, $460°C \leq T \leq 625°C$, the low melting point itself appears to be best correlated with the behavior of the jet.

The metals selected for this investigation are presented in Table 1 with their physical properties.

7

Table 1

Physical Properties of Liner Metals

Metal Type	Tensile Strength kg/cm² x 10³	Compressive Strength kg/cm² x 10³	Elongation Percent	Hardness Rockwell	Modulus of Elasticity kg/cm² x 10⁵	Modulus of Rigidity kg/cm² x 10⁵	Metal Density gm/cm³	Melting Point °C
Aluminum T-3, 2011	3.866	3.023	15	95E	7.171	2.671	2.82	535-643
Aluminum T-6, 7075	5.835	5.132	17	100E	-----	2.742	2.80	476-637
Brass (yellow)	4.288	3.515	23	84K	7.382	2.742	8.47	904.4
Monel	6.679	5.273	27	96B	18.279	6.679	8.84	1300.0
Maraging Steel Vascomax 250	9.8	10.43	19	29C	18.55	7.14	8.0	--
Copper	2.39	-----	45-50	34RE	11.95	-----	8.96	1083.0

Percentage Composition of the Metals

Aluminum T-3	Al	93.5%, Cu 5.5%, Pb 0.5%, Bi 0.5%
Aluminum T-6	Al	91.2%, Zn 5.5%, Mg 2.5%, Cu 1.5%, Cr 0.3%
Yellow Brass	Cu	65%, Zn 35%
Monel	Ni	66.26%, Cu 31.26%, Fe 1.12%, Al 0.12%, Si 0.7%, C .19%, Mn 0.94%
Steel	Ni	18.5%, Co 7.5%, Mo 7.5%, Fe 68.37%, others 0.82%
Copper	Cu	+99%

2. <u>Apex angle</u>. Conical liners were used in this study because they are easy to machine and have proven to be one of the most effective geometries. Brimmer (19) has shown that for metallic targets the optimum cone angle for maximum penetration is approximately 60°, whi . 'ʃ the cone angle employed in this study.

3. <u>Liner thickness</u>. The liners were designed with optimum thickness (l_{th} optimum) which was obtained by using the relationship suggested by Winn (20):

$$l_{th} \text{ Optimum} = \frac{(l_{th} \text{ Optimum Copper})(\text{Density of Copper})}{(\text{Density of Metal})} \qquad (8)$$

The optimum thickness of the copper liner was taken as 0.105 cm for 60° cones of 5 cm diameter.

The average weights and thickness of the liners were:

Metal	Weight (gm)	Liner Thickness (cm)
Aluminum 2011 (T-3)	32.5 ± 0.25	0.3500 ± 0.002
Aluminum 7075 (T-6)	32.0 ± 0.25	0.3430 ± 0.002
Yellow Brass	36.1 ± 0.25	0.1150 ± 0.002
Maraging Steel	34.7 ± 0.25	0.1161 ± 0.002
Monel	34.2 ± 0.25	0.1065 ± 0.002
Copper (42 degree)	47.9 ± 1.00	0.1050 ± 0.002

4. <u>Charge Dimensions</u>. The charge length must be sufficient to provide a fully developed detonation front before it makes contact with the apex of the liner. Baum (2) points out that the minimum height of the charge for which its active portion attains its limiting value for a cylindrical charge is equal to $H_{lim} = CR + h$. Thus, H_{lim} for conical liners is approximately equal to 2 cone diameters. Framing camera photographs show that the detonation front for C-4 is fully developed when it contacts the cone for a length of 2 cone diameters. Based on these observations and the literature review a standard charge length of 2 cone diameters was used, which in the present investigation equalled 10 cm. The charge to cone diameter ratio was 1.04.

5. <u>Type of Explosive</u>. The characteristics of explosives commonly employed in shaped charge studies are presented in Table 2. The most desirable properties are high detonation pressure and velocity. Composition C-4 (Table 3) possesses these characteristics and is easy to load by hand. The explosive

9

Table 2 (Ref. 19)

Shaped-Charge Explosives

Designation	Loading Density g/cc 25°C	Detonation Velocity Meters Per Sec.	Relative Power*	Impact Sensi- tivity**	Stability***	Remarks
Cast Pentolite 50/50	1.65	7,500	126	12	moderately stable	Used chiefly in shaped charges; penetration is 90-95% that of 65/35 Cyclotol. More sensitive than 65/35 Cyclotol.
Cast Cyclotol 65/35	1.71	7,995	134	--	fairly stable	Better for filling small shaped charges
Cyclotol 70/30	1.725	7,790	135	14	fairly stable	One of the most effective shaped charge explosives; too viscous to load small shaped charges.
Cast RDX	1.65	8,180	150	8	fairly stable	Samples stored 2.5 yr. at ordinary temp. found to be perfect. Germans used pressed pre-formed pellets in shaped charges (Comp. A: RDX 90% wax 10%); not used alone in shaped charges.
Cast Comp. B	1.88	7,840	133	14	very stable	About 20% more effective than cast TNT; high shaped charge efficiency; good loading characteristics; sensitive to shock.

10

Table 2 (cont'd)

Shaped-Charge Explosives

Designation	Loading Density g/cc 25°C	Detonation Velocity Meters Per Sec	Relative Power*	Impact Sensitivity**	Stability***	Remarks
Plastic Comp. C-2 (DuPont)	1.57	7,660	126	--	--	Hardens when stored at elevated temperature.
Plastic Comp. C-3	1.60	7,625	126	14	moderately stable	Comp. C modified to provide a good explosive for molded and shaped charges; tends to harden in storage; special packaging needed to prevent exudation even at 55°F.
Plastic C-4	1.59	8,578	130	19	stable	Composition C-4 has been developed to improve the instability and hygroscopy of C-3. Will not undergo exudation at 77°C.
Castable, similar to Comp. B PTX-2	1.70	8,065	138	--	stable	Developed by Picatinny Arsenal as castable filling for shaped charges.
Small charges pressed; medium & large charges, cast TNT	1.56 cast 1.56 pressed	6,640 6,825	100	14-15	very stable	Used for blasting, demolition.

11

Table 2 (cont'd)

Shaped-Charge Explosives

Designation	Loading Density g/cc 25°C	Detonation Velocity Meters Per Sec	Relative Power*	Impact Sensitivity**	Stability***	Remarks
Cast HBX	1.65	7,100	113	8	stable	Intended as replacement for Torpex in depth bombs; generation of hydrogen may deform cavity.
Cast Torpex 2	1.71	7,200	116	6	very stable	Mainly used in underwater ordnance; generation of hydrogen may deform cavity.
Astrolite G Liquid	1.4	8,600	174	--	--	Has a very high gas volume. Suitable for shaped charges and fragment acceleration
Astrolite A-1-5 Liquid	1.6	7,500	237	--	--	It is a white explosive and melts at 273°-280°C. It is very similar to cyclonite in sensitivity, brisance and strength.
Cast HMX	1.84	9,124	150	9	--	

*   Power of an equal volume of explosive relative to TNT (=100) based on the ballistic mortar.
** Picatinny Arsenal apparatus.
*** Those classified as moderately stable will survive all but drastic tropical storage; stable and very stable will survive this.

12

Table 3

Properties of Composition C-4

Composition C-4	Percentage	Empirical Formula	Heat of Formation Kcal/Mole
RDX	91.0	$C_3H_6N_6O_6$	-18.3
Polyisobutylene	2.1	C_4H_8	-19.7***
Motor Oil (SAE 10)	1.6	CH_2	- 4.9
Di-(2-ethylhexyl) Sebacate	5.3	$C_{26}H_{50}O_4$	-306.9***
	100.0		

Empirical formula for C-4 $C_{1.80}H_{3.60}N_{2.45}O_{2.50}$

Heat of formation for C-4   -126.1 Kcal/mole

Heat of reaction for C-4*   983 cal/g

For this data, a density of 1.59 g/cm^3, and the B.K.W. equation of state, the following parameters were computed:**

Density	1.59 g/cm^3
Detonation velocity	8,578 m/sec
Particle velocity	2,320 m/sec
Sound velocity	6,258 m/sec
Detonation pressure	312,333 atm
Detonation temperature	3,374°k
Total gas	34.667 moles/kg of explosives
Total solid (carbon)	12.176 moles/kg of explosive

* Experimental value from oxygen bomb calorimeter measurements, personal communication from personnel at Picatinny Arsenal.

** Operator's Manual for RUBY, UCRL 6815 or TID 4500.

*** Personal communication from Dr. D.S. Wulfman, UMR.

was loaded at a density of 1.6 gm/cc at which it has a theoretical velocity of 8611 m/sec and a pressure of 327,069 kg/cm^2. A mechanical device which applied a controlled pressure was used to ensure uniform loading of the explosive, and a No. 8 blasting cap was adequate for detonation.

6. Target Material (Table 4). Initial tests were performed on cast concrete blocks (Table 5) and rhyolite (Table 6). However, these materials were too weak and brittle, and it was not possible to obtain hole dimensions. Missouri red granite was used as the target material for most of the data obtained in this investigation.

Table 4

Physical Properties of Target Materials

Rock Type	Density g/cc	Impact Hardness	Compressive Strength g/cm^2/10^4	Compression Wave Velocity cm/sec x 10^5	Apparent Porosity %
Concrete	2.069	31*	84.0	4.45*	18.69
Rhyolite	2.620	--	337.0	----	0.16
Missouri Red Granite	2.60	53*	119.0	4.52*	0.4

*Reference (21)

Table 5

Penetration in Concrete by 60° Liners

Charge No.	Liner Thickness cm	Standoff cm	Penetration cm
35 S	0.1161	20.0	22.5
36 S	0.1161	15.0	38.5
37 S	0.1161	5.0	31.5
38 S	0.1161	10.0	17.5
49 Al6	0.3480	15.0	39.6
50 Al6	0.3480	20.0	22.8
53 Al6	0.3480	15.0	35.5

S   Maraging Steel (Vascomax 250)
Al6 Aluminum 7075 (T-6)

14

Table 6

Penetration in Rhyolite by 60° Liners

Charge No.	Liner Thickness cm	Standoff cm	Penetration cm
42 B	0.115	5.0	10.0
43 B	0.115	10.0	20.0
44 B	0.115	17.5	15.0
45 B	0.115	29.0	22.5
52 A16	0.348	20.0	10.0
54 A16	0.348	15.0	10.0

B Yellow Brass
A16 Aluminum 7075 (T-6)

Table 7

Optimum Standoff

Aluminum 2011 (T-3)	20.0 cm	or	4.0 CD
Aluminum 7075 (T-6)	22.5 cm	or	4.5 CD
Yellow Brass	15.0 cm	or	3.0 CD
Monel	17.5 cm	or	3.5 CD
Maraging Steel	10.0 cm	or	2.0 CD
Copper (42 degree)	16.25 cm	or	3.25 CD

IV. EXPERIMENTAL RESULTS

A. <u>Penetration Studies</u>. Penetration depths not including spallation were measured with a graduated metallic probe. Holes were assumed to be a right circular cone, and spalled thickness was measured as accurately as possible. The hole was plotted to scale and the slant surface extended to the original rock surface. The radius so obtained was taken as the effective value at the surface.

An expendable template was designed to centrally locate the detonator and produce a symmetrical detonation front (Figure 4). Charges were fired at variable standoff to obtain the optimum value (Table 7). Optimum standoff was employed in the experiments for measurement of the rate of penetration into granite by jets from liners having 42, 55, and 75 degree apex angles (Table 8).

Penetration in Granite

<u>Aluminum 2011 (T-3)</u>. Jets showed considerable variation in penetration, which is attributable to nonhomogeneities in the rock and other experimental variables. Liners with 42, 55, and 75 degree apex angles gave less penetration than those with 60 degree apex angle. One liner was annealed for 20 hours at 413 degrees C, but this resulted in less penetration. Maximum penetration was obtained at a standoff of 20.0 cm (4.0 cone diameters). (Figure 5, Table 9).

<u>Aluminum 7075 (T-6)</u>. A gradual increase in penetration with standoff occurs from 4.0 to 4.5 cone diameters. Penetration by jets from 42, 55, and 75 degree liners when fired at optimum standoff for 60 degree liners showed less penetration. One liner was annealed at 413 degrees C for 20 hours, was fired at the optimum standoff, and showed a slight increase in penetration. (Figure 6, Table 10).

<u>Yellow Brass</u>. Yellow brass gave greater penetration than all other liners tested. Liners having 42, 55, and 75 degree apex angles when fired at the best standoff for the 60 degree liners gave less penetration than the 60 degree liners. One of the 60 degree liners was annealed for two hours at 413 degrees C. The annealed liner gave less penetration than the nonannealed liners. Maximum penetration was obtained at a standoff of 15.0 cm.

Three shots were fired in rhyolite and about 20.0 cm of penetration was observed at 10.0 cm standoff. The reliability of the penetration data obtained is questionable due to extensive fracturing of the target, because of the brittle nature of the rhyolite and microfractures present from the quarry blasting. (Figure 7, Table 11).

16

Table 8

Penetration in Granite - 60° Liners at Optimum Standoff

Charge No.	Apex Angle	Liner Thickness	Stand-off	Penetration	Hole Radius	Hole Volume
	deg	cm	cm	cm	cm	cc
155 T3	42	0.2750	20.0	10.1	-	+
11 T3	55	0.2750	20.0	9.3	3.5	119.3^c
57 T3	60	0.3500	20.0	15.0	-	+
154 T3	75	0.3160	20.0	9.9	1.2	14.93
157 T6	42	0.2750	22.5	12.2	0.9	10.35
22 T6	55	0.2750	22.5	11.1	0.5	5.70
G T6	60	0.3480	22.5	13.2	-	-
34 T6	75	0.3160	22.5	9.1	-	-
19 M	42	0.1000	17.5	12.7	1.3	11.3
21 M	55	0.1000	17.5	12.3	0.7	6.3
65 M	60	0.1065	17.5	17.0	1.8	15.6
32 M	75	0.1000	17.5	9.7	0.9	8.2
159 B	42	0.1000	15.0	11.5	1.3	11.3
160 B	55	0.1000	15.0	15.3	0.8	6.3
100 B	60	0.1150	15.0	17.4	1.7	26.2
25 B	75	0.1500	15.0	13.9	0.9	22.5
18 S	42	0.1000	10.0	11.8	0.7	6.0
16 S	55	0.1000	10.0	11.7	1.1	14.8
40 S	60	0.1161	10.0	16.0	1.5	37.7
30 S	75	0.1500	10.0	8.0	0.7	4.1

+ = Crater (no hole radius could be measured)

T3 = Aluminum 2011 (T3)

T6 - Aluminum 7075 (T6)

M = Monel
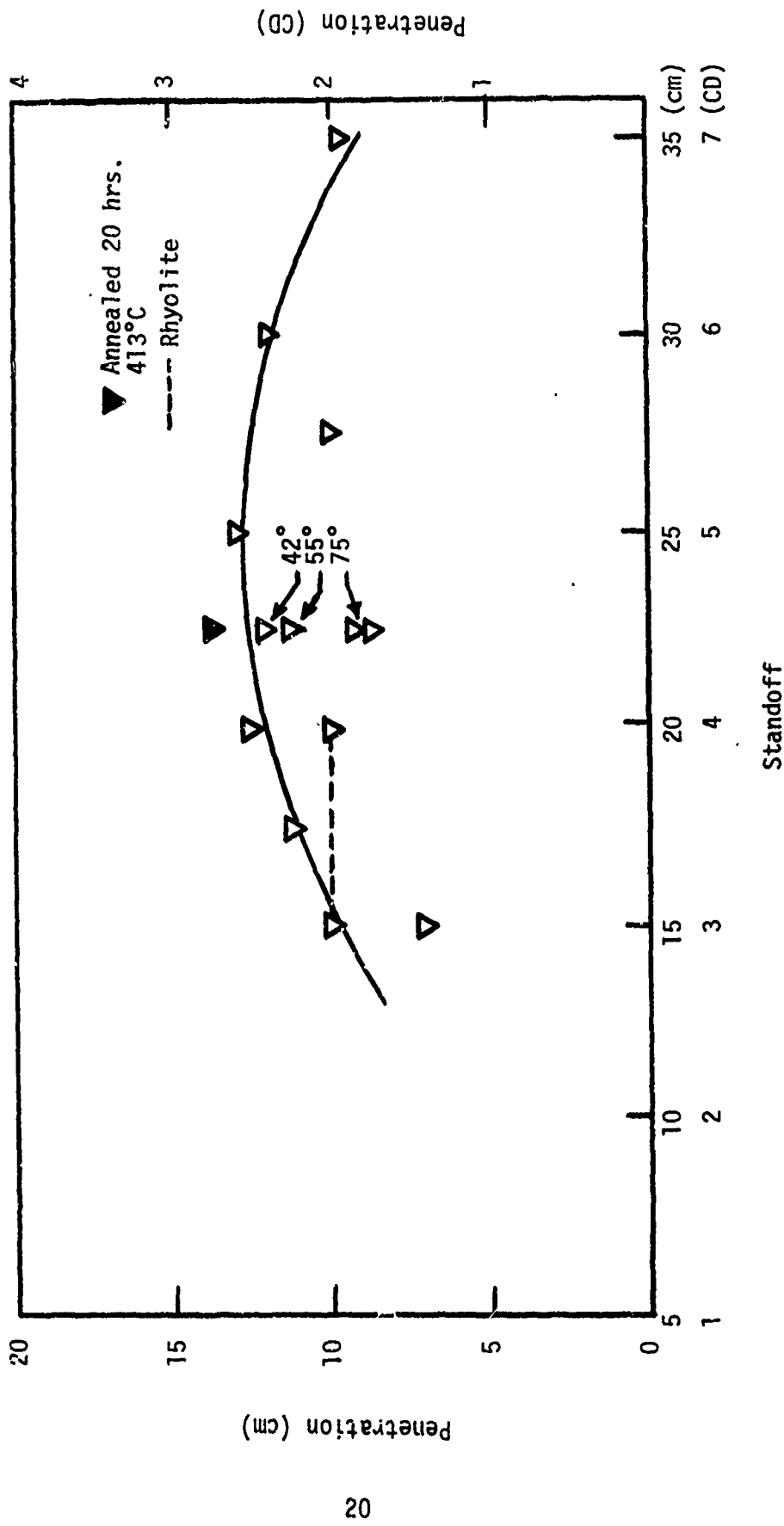
B = Brass

S = Steel

C = Crater

G = From graph

17
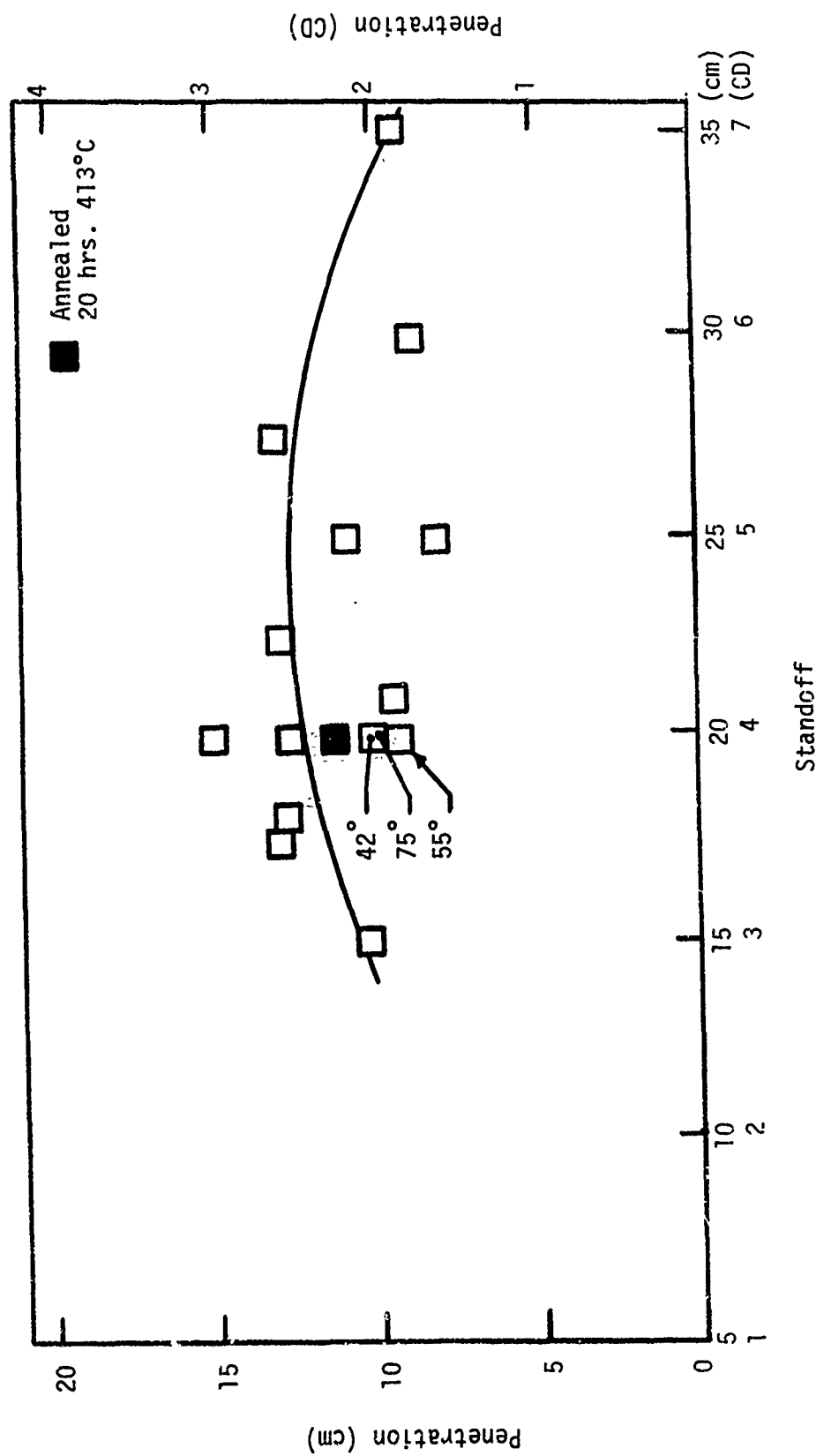
Figure 5. Penetration in Missouri Red Granite – 60 Degree
Aluminum 2011 (T-3) Liners

Table 9

Penetration in Granite - 60° Aluminum 2011 (T-3) Liners

Charge No.	Standoff		Penetration		E.R.*	H.V.**
	cm	CD^+	cm	CD^+	cm	cc
56	15.0	3.0	10.3	2.06	***	$-$
60	17.5	3.5	13.0	2.60	2.5	85.1^{++}
62	18.0	3.8	12.8	2.56	***	..
57	20.0	4.0	15.0	3.0	***	$-$
118	20.0	4.0	12.7	2.54	1.0	13.3
115	21.0	4.2	9.5	1.90	***	$-$
61	22.5	4.5	13.0	2.60	***	$-$
59	25.0	5.0	8.0	1.60	***	$-$
119	25.0	5.0	10.2	2.16	2.5	66.8^{++}
58	27.5	5.5	13.0	2.60	2.0	54.5
116	30.0	6.0	8.8	1.76	***	$-$
120	35.0	7.0	9.2	1.84	2.0	38.5
A130	20.0	4.0	11.2	2.24	1.2	16.9

+ = Cone diameters

* E.R. = Effective hole radius

**H.V. = Hole volume

*** = Hole was shattered

++ = Conical crater with smooth walls

A = Annealed liner

Figure 6. Penetration in Missouri Red Granite – 60 Degree
Aluminum 7075 (T-6) Liners

Table 10

Penetration in Granite - 60° Aluminum 7075 (T-6) Liners

Charge No.	Standoff		Penetration		E.R.*	H.V.**
	cm	CD+	cm	CD+	cm	cc
54	15.0	3.0	10.0	1.40	1.4	29.3
89	17.5	3.5	11.2	2.24	0.9	8.5
55	20.0	4.0	12.5	2.50	***	
87	22.5	4.5	8.5	1.70	4.0	142.4++
83	25.0	5.0	13.0	2.60	4.0	217.8++
88	27.5	5.5	10.0	2.00	1.0	11.0
84	32.5	6.5	12.0	2.40	***	
90	35.0	7.0	9.8	1.96	2.0	41.0++
A131	22.5	4.5	13.7	2.74	0.8	9.2

+ CD = Cone diameters

* E.R.= Effective hole radius

**H.V.= Hole volume

*** = Hole was shattered

++ = Conical crater with smooth walls

A = Annealed liner

****

Table 11

Penetration in Granite - 60° Yellow Brass Liners

Charge No.	Standoff		Penetration		E.R.*	H.V.**
	cm	CD+	cm	CD+	cm	cc
98	5.0	1.0	13.0	2.6	***	--
99	10.0	2.0	13.0	2.6	1.4	26.7
48	12.5	2.5	16.5	3.3	0.8	11.1
100	15.0	3.0	17.4	3.5	1.7	52.7
103	17.5	3.5	14.5	2.9	1.0	15.2
101	20.0	4.0	10.8	1.2	0.7	5.5
104	5.0	1.0	12.2	2.4	0.7	6.3
A129	15.0	3.0	14.6	2.9	0.8	8.6

+ = Cone diameters

* E.R.= Effective hole radius

**H.V.= Hole volume

*** = Hole was shattered

A = Annealed liner
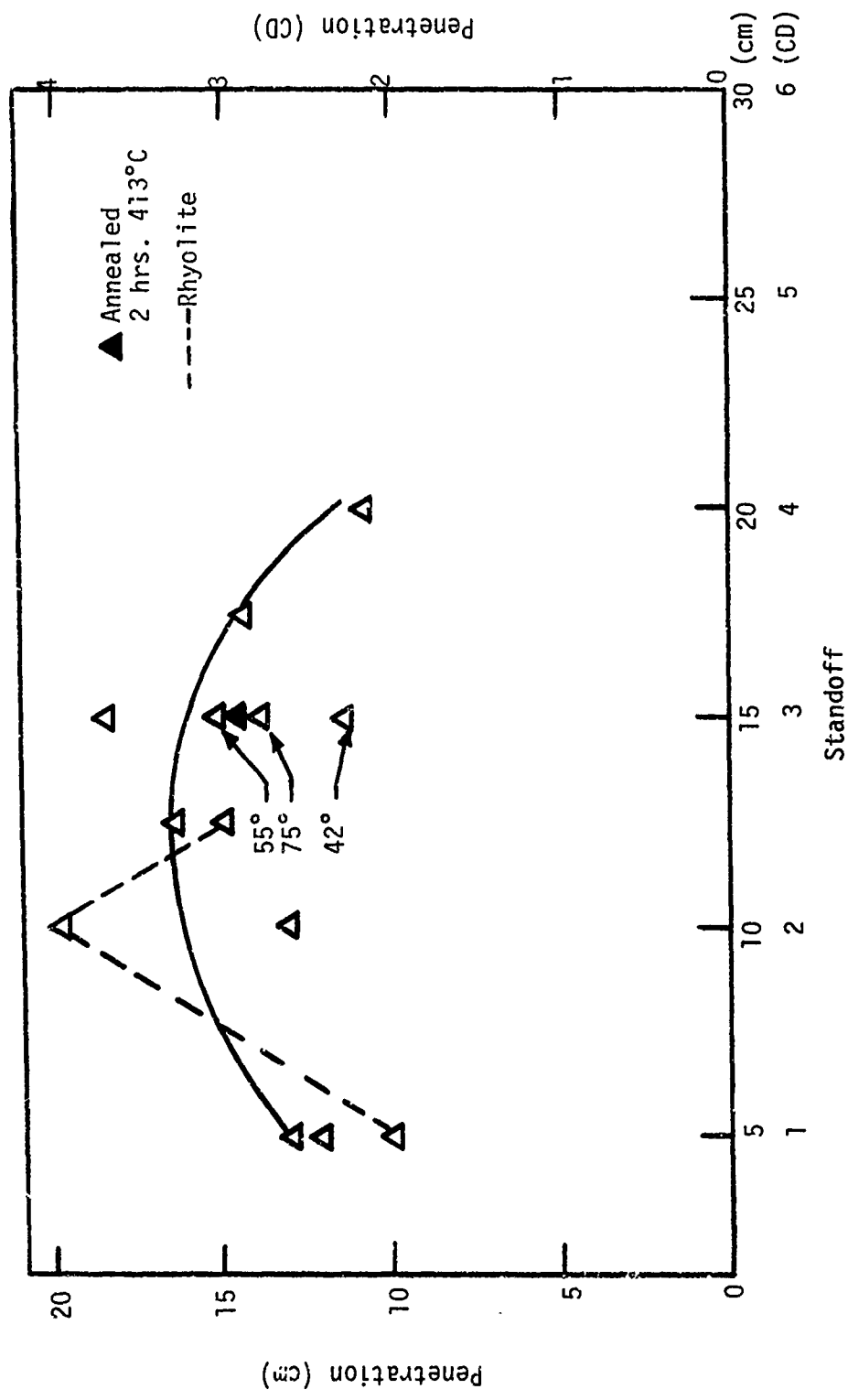
Figure 7. Penetration in Missouri Red Granite - 60 Degree
Yellow Brass Liners

22

Monel Liners, 60 degree. Penetration by jets from 42, 55, and 75 degree liners was less than that for 60 degree liners. One cone was annealed at 871 deg C for two hours, and gave less penetration than the nonannealed cones. One low value of penetration is attributed to large quartz crystals in the target. The curve is somewhat similar to yellow brass with less scatter than for brass. (Figure 8, Table 12).

Maraging Steel Liners, 60 degree. The best penetration was obtained at 10.0 cm standoff. The 42, 55, and 75 degree liners gave less penetration than 60 degree liners. Since the penetration trend was not promising and this metal required greater machining time, only three tests were made. (Figure 9, Table 13).

Copper Liners, 42 degree. Fifteen jets were fired into granite using 42 degree copper liners with flanges, and nominal scatter was observed in the penetration data. Flanges were removed from 5 cones, and no significant effects were observed. For this metal, penetration in granite seems to be less sensitive to standoff compared with most other metals. Some of the scatter in data was probably due to the variations in liner mass (46.8-49.5 gm) and imperfections in manufacture. (Figure 10, Table 14).

Summary. The general trend of curves for all the metals is similar (Figure 11), i.e., an increase in penetration with increase in standoff in accord with theory until a maximum is reached, followed by a decrease in penetration. Aluminum requires a greater standoff than other metals. This may be due to the cohesiveness of aluminum which is body-center cubic. All jets have a velocity gradient, with the highest velocity at the tip. Hence, the breakup time of aluminum may be greater which would permit the formation of a longer cohesive jet. Except for aluminum all metals show maximum penetration at about 2.5 to 3.5 cone diameters standoff, whereas optimum standoff for aluminum is between 4.0 and 5.0 cone diameters. Except for aluminum 7075 (T-6) all the annealed liners gave less penetration than nonannealed liners. The scatter in the penetration data was due to the anisotropic nature of the target, variables in liner properties, loading density and other factors.
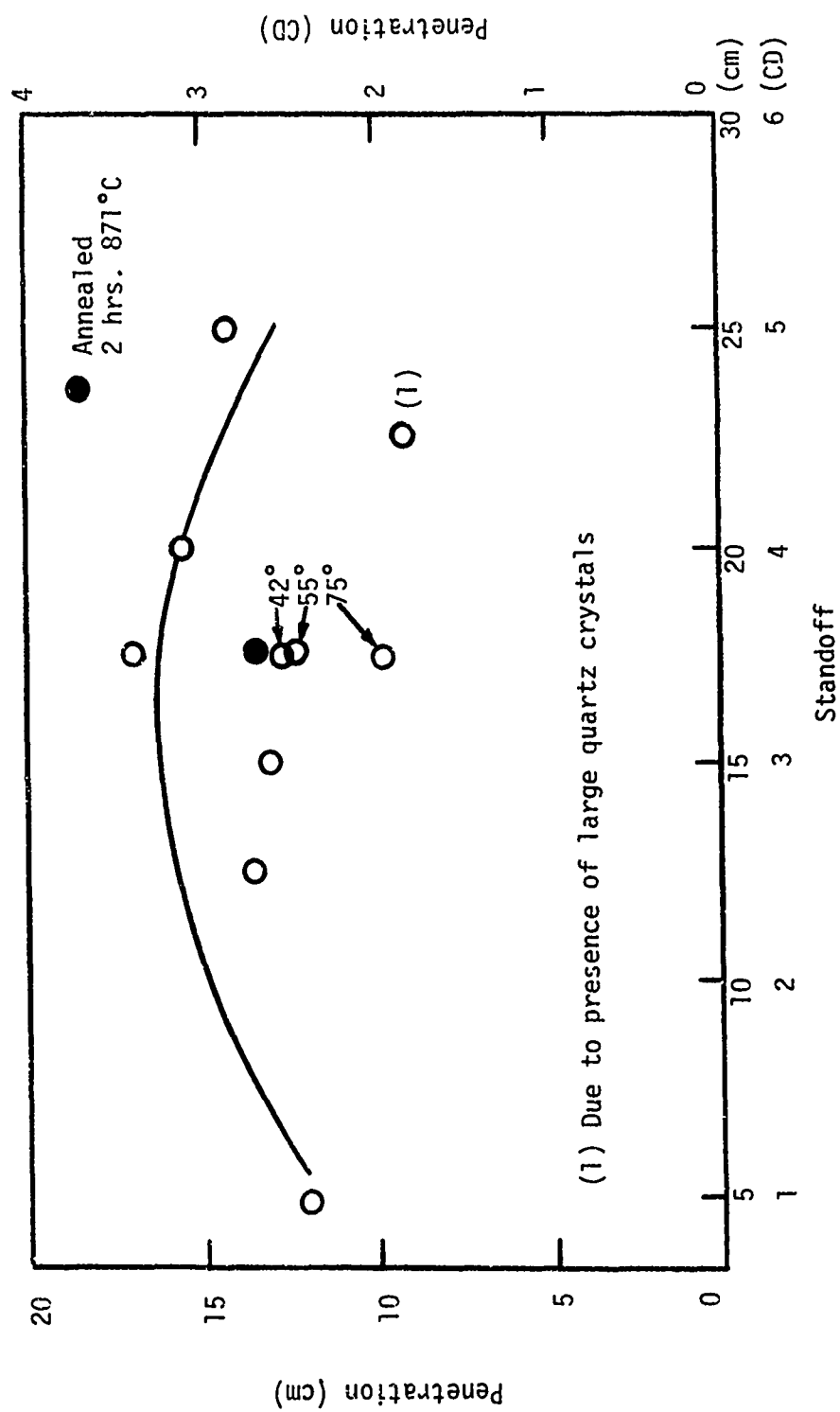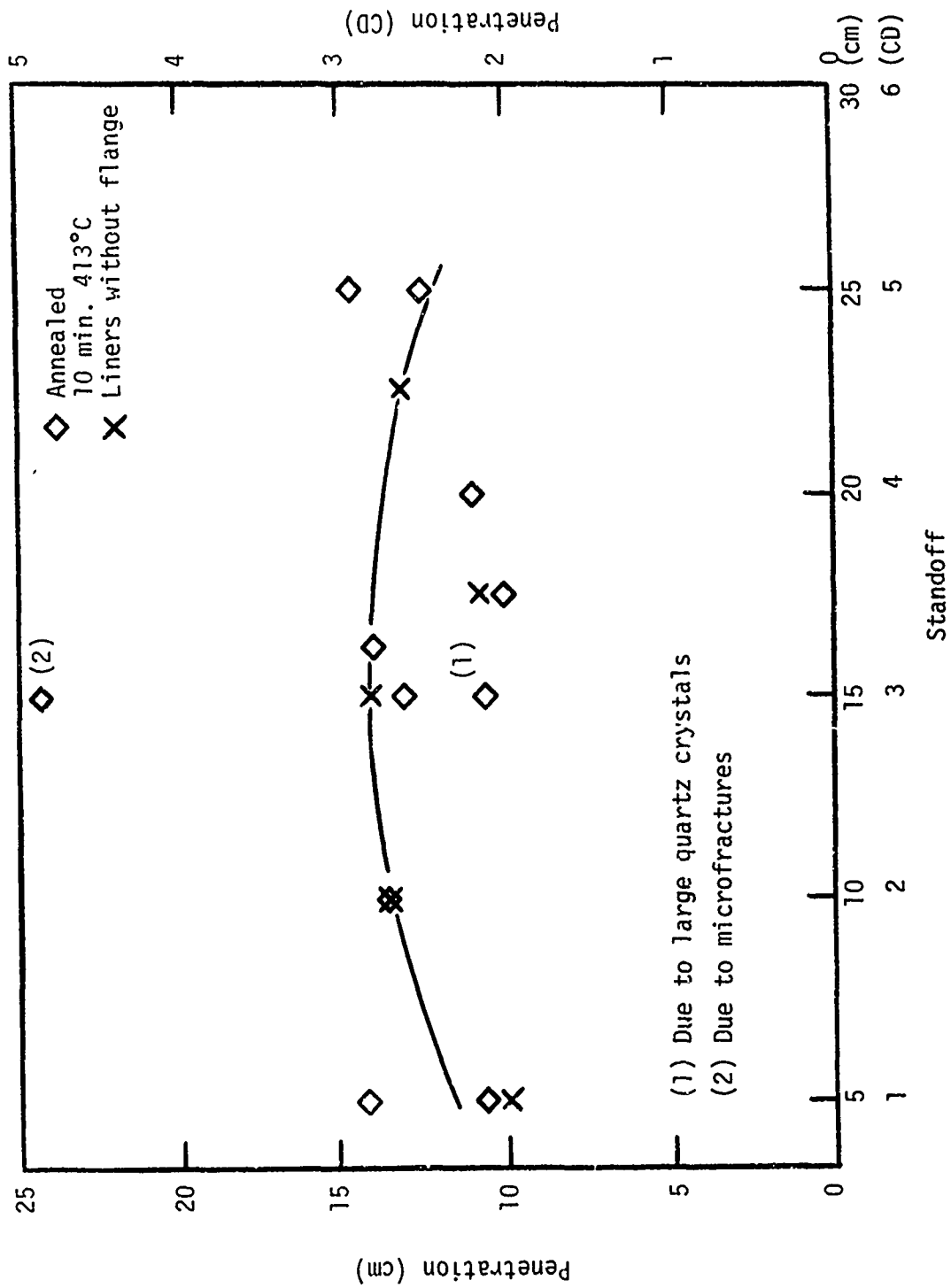
23

Figure 8. Penetration in Missouri Red Granite - 60 Degree
Monel Liners

Table 12

Penetration in Granite - 60° Monel Liners

Charge No.	Standoff		Penetration		E.R.*	H.V.**
	cm	CD+	cm	CD+	cm	cc
63	5.0	1.0	12.0	2.4	***	---
64	12.5	2.5	13.5	2.7	1.5	31.8
67	15.0	3.0	13.0	2.6	1.0	13.6
65	17.5	3.5	17.0	3.4	1.8	57.7
66	20.0	4.0	9.0	1.8	4.0	150.8++
68	20.0	4.0	15.5	3.1	***	
69	25.0	5.0	14.1	2.8	1.0	14.8
A128	17.5	3.5	13.4	2.7	0.9	11.4

+   CD = Cone diameters

*   E.R. = Effective hole radius

** H.V. = Hole volume

***   = Hole was shattered

++   = Smooth wall conical crater

A   = Annealed liner

****

Table 13

Penetration in Granite - 60° Maraging Steel
(Vascomax 250) Liners

Charge No.	Standoff		Penetration		E.R.*	H.V.**
	cm	CD+	cm	CD+	cm	cc
39	5.0	1.0	14.5	2.90	2.0	60.74++
40	10.0	2.0	16.0	3.20	1.5	37.7
41	15.0	3.0	10.0	2.00	4.0	167.5++

+   CD = Cone diameters

*   E.R. = Effective hole radius

** H.V. = Hole volume

++   = Smooth wall conical crater

25
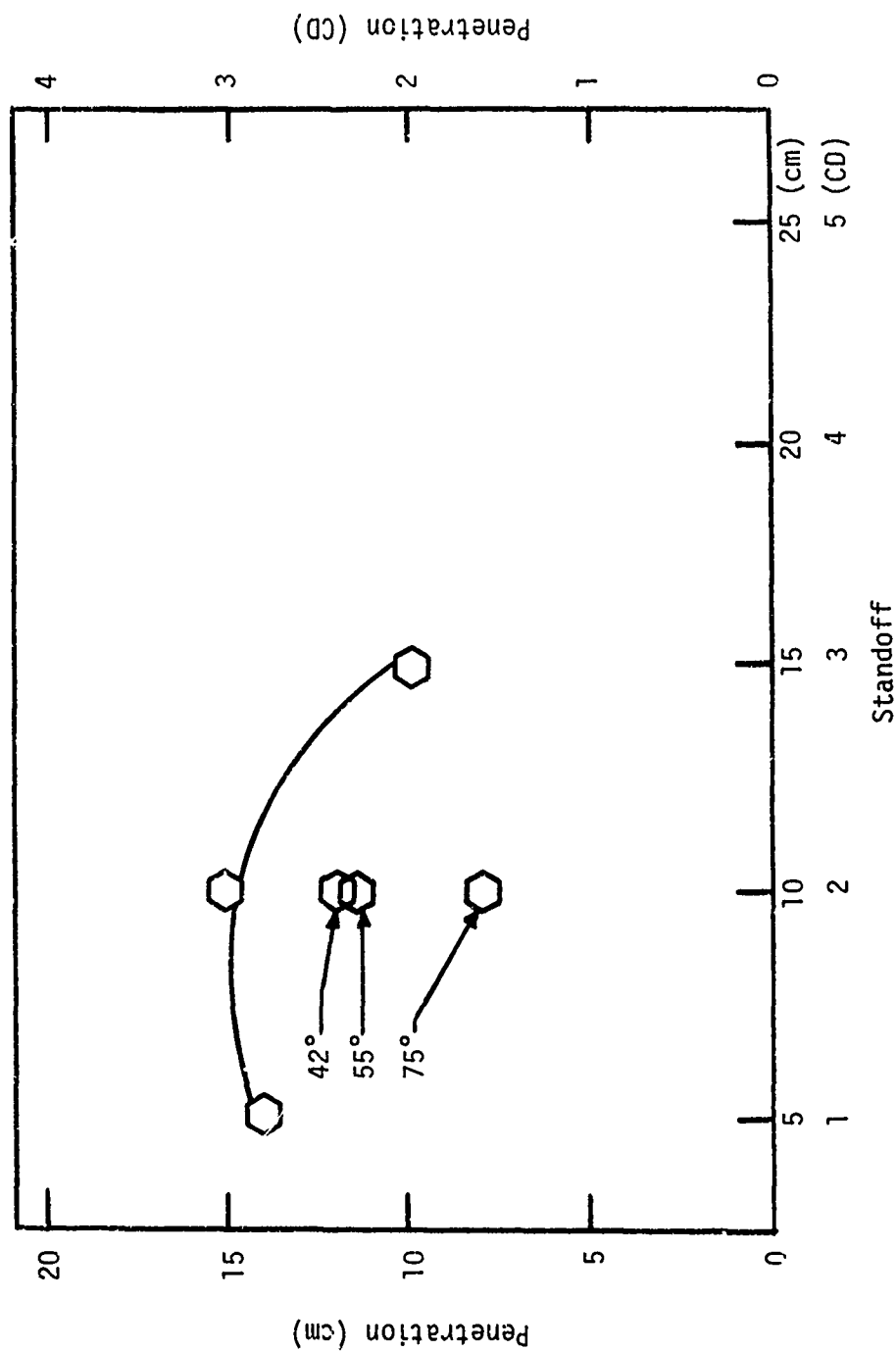
Figure 9. Penetration in Missouri Red Granite - 60 Degree
Maraging Steel Liners

Figure 10. Penetration in Missouri Red Granite – 42 Degree Copper Liners

Table 14

Penetration in Granite - 42° Copper Liners

Charge No.	Standoff		Penetration		E.R.*	H.V.**
	cm	CD+	cm	CD+	cm	cc
106	5.0	1.0	14.5	2.90	1.0	18.4
108	10.0	2.0	13.5	2.70	0.9	11.5
107	15.0	3.0	24.5	4.90	1.2	36.9
110	20.0	4.0	11.0	2.20	0.6	4.2
112	15.0	3.0	10.2	2.04		
109	25.0	5.0	12.5	2.50	0.8	8.4
124	5.0	1.0	10.6	2.42	0.9	9.0
125	15.0	3.0	13.2	2.64	0.8	8.8
126	17.5	3.5	10.0	2.00		
128	25.0	5.0	14.8	2.96	0.9	11.2
-145	5.0	1.0	10.0	2.00	1.0	10.5
-146	10.0	2.0	13.6	2.72	1.0	14.2
-147	15.0	3.0	14.3	2.86	1.0	15.0
-148	17.5	3.5	10.8	2.16	1.1	13.7
-149	22.5	4.5	13.2	2.64	1.1	16.7
A127	16.3	3.3	14.1	2.82	0.9	12.0

+   CD = Cone diameters

*   E.R. = Effective hole diameter

** H.V. = Hole volume

-     = Copper liners without flange

A   = Annealed liner
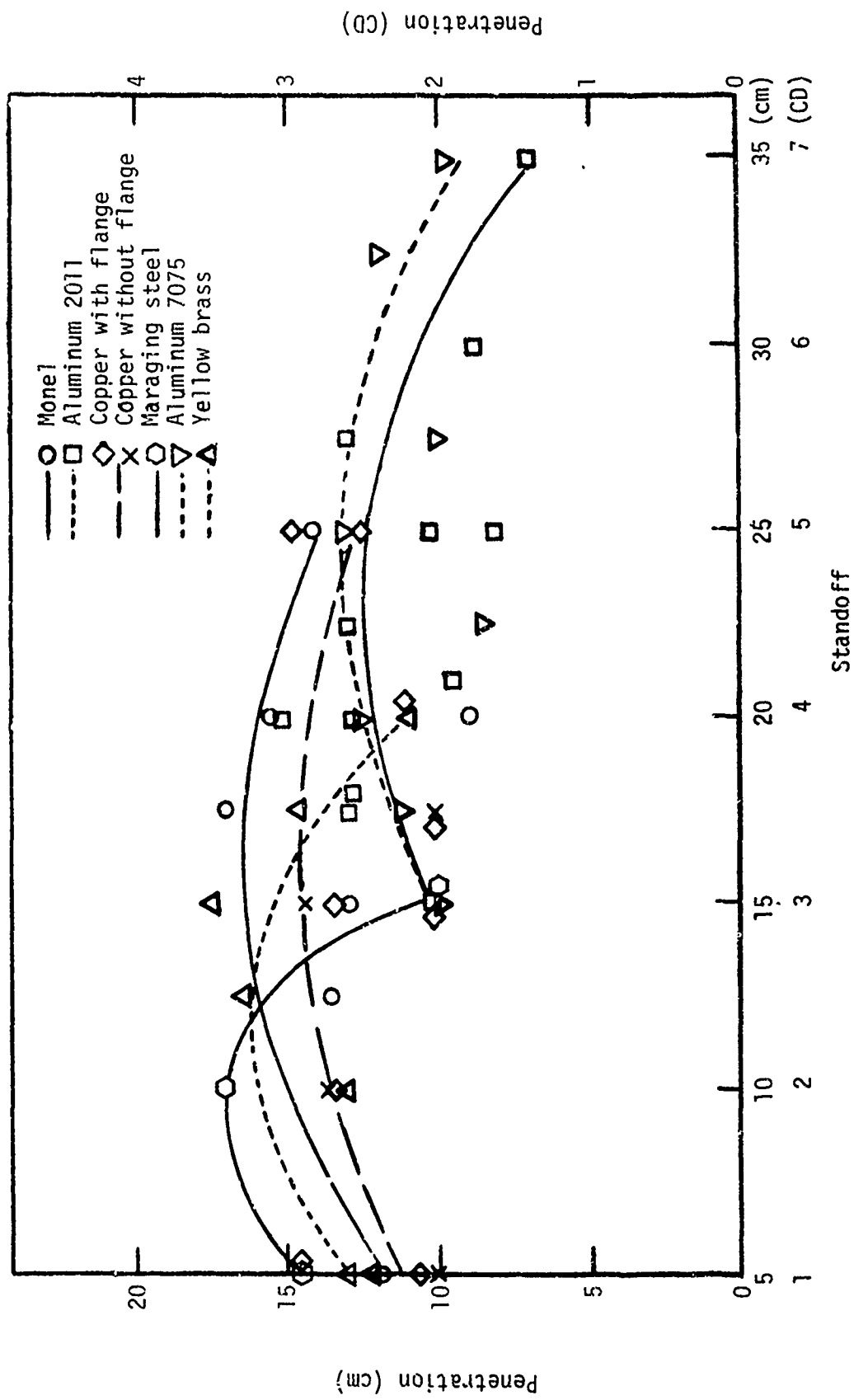
Figure 11. Penetration in Granite – six metals

29

The granite blocks had small joints and the grain structure was non-uniform. Early tests with concrete had shown that joints have an effect on the penetration. The abnormally large penetration observed with copper liner (charge No. 107, penetration 24.5 cm) could have been due to microfractures in the granite from previous testing in the block.

Copper jets do not exhibit a superior ability for penetration in granite as they do in steel (19). The order of effectiveness for penetration in granite is likewise not the same for all metals as in steel, although the steel jets reported by Brimmer (19) were probably of different material than the steel jets utilized in this study.

B. Jet Characteristics and Jet Tip Velocity. Attempts were made to photograph jets moving through air and helium atmospheres with a framing camera (Figure 12). The jet was visible for the first few microseconds, then the interactions between the shock waves created by the jet tip and the atmosphere or the target obscured the jet and the reaction of the target face.

NOT REPRODUCIBLE
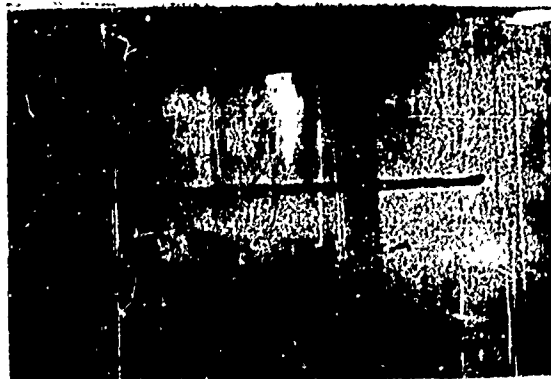
Figure 12.   Shaped Charge Jet 26 Microseconds
after Initiation

Flash X-ray equipment employed by several investigators (2, 18, 25) has shown that jets are continuous and cohesive for a short time. Subsequently the jet breaks up into small particles of approximately the same length. On the basis of published date (14, 15), it is estimated that the jets formed in this investigation remain continuous for the following approximate times:

30

Aluminum	40-55 μsecs
Copper	50-60 μsecs
Monel	50-60 μsecs
Steel	50-60 μsecs
Yellow Brass	50-60 μsecs

Pin oscilloscope techniques were employed to obtain jet tip velocities through air and granite. Two shots per metal were fired to obtain the rate of penetration and jet tip velocity. The jet tip velocity through air is given below:

Aluminum 2011 (T-3)	8.09 mm/μsec.
Aluminum 7075 (T-6)	7.91 mm/μsec
Copper	8.87 mm/μsec
Monel	9.83 mm/μsec
Steel	7.69 mm/μsec
Yellow Brass	8.87 mm/μsec

The rate of penetration into granite was obtained by placing pin sets between granite slabs. The velocity decreased rapidly in the first few centimeters (Figure 13) and then decreases more slowly until maximum penetration (minimum penetration velocity) is reached.

From the observed data there does not appear to be a direct correlation between either tip velocity or minimum penetration velocity and jet density. The scatter of data may have been due to the inhomogeneity of the rock, erratic performance of probes or subnormal performance of given charges.

C. Mechanics of Penetration. Penetration involves local shock compression of the materials to very high pressures, possibly accompanied by some melting and vaporization of the target material. The process of hole enlargement involves extremely high stresses and strains, as well as ejection of material from the hole.

A shock receding into the (continuous) oncoming jet is carried below the original target surface when the jet velocity exceeds the velocity of the shock wave generated in the jet. This critical velocity is a function of the densities and the compressibilities of the jet and target material. As the jet continues to penetrate, the shock wave into the target precedes the jet-target interface. Rarefaction from the free surface of the target and the jet modify the shock system and the shock becomes approximately conical in shape inside the target. To reduce the probability of shorting out of the

31
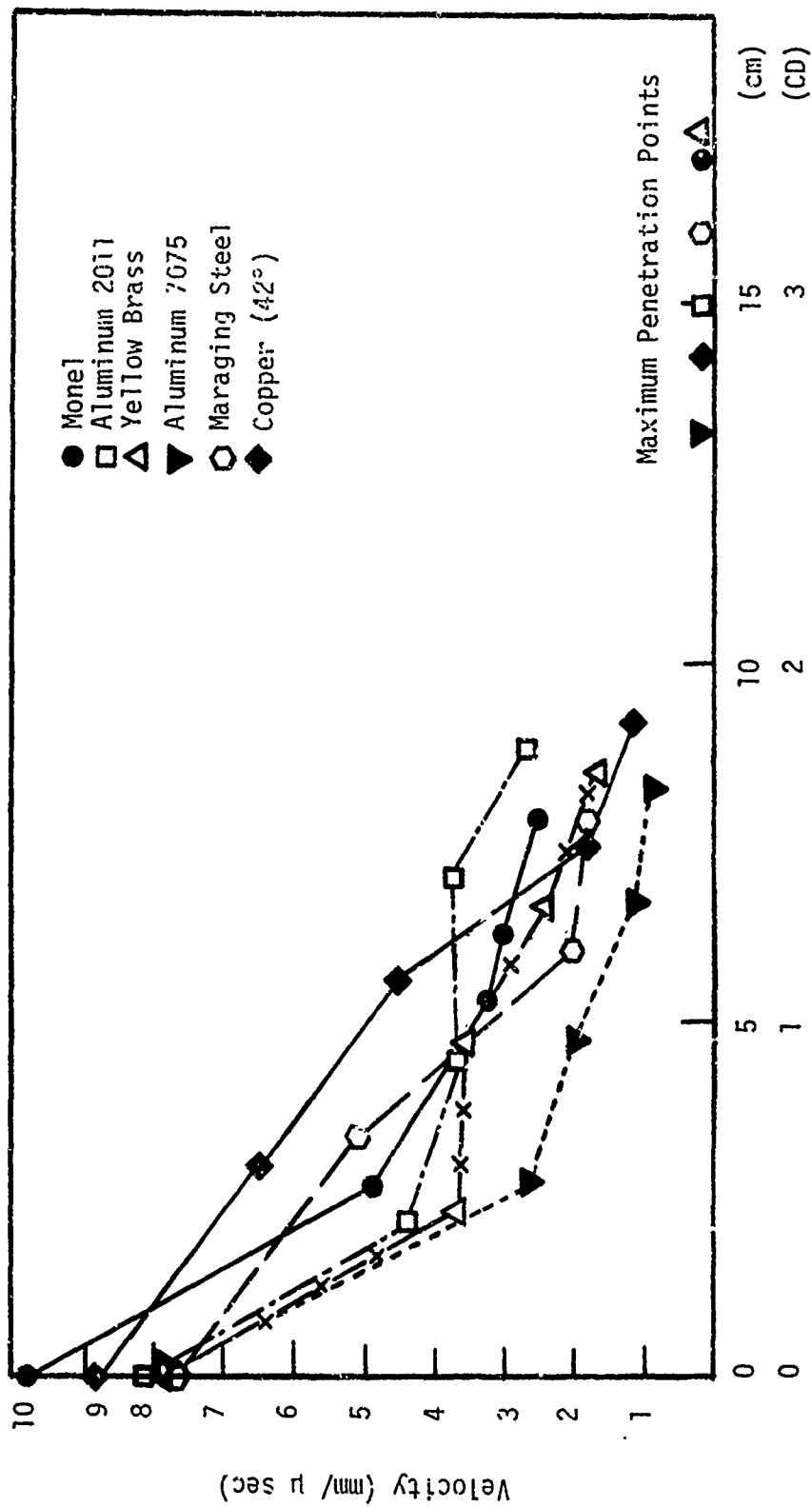
Figure 13. Jet Tip Velocity Through Granite Blocks

32

pinsets by the shock waves rather than by the jet during rate of penetration measurements the target slab assembly was placed inside a sand filled container,

Target Effects. The manner in which rock behaves under jet impact has not yet been fully explained. Bowden (22) has suggested that five different forms of deformation take place in the target material when subjected to high velocity impact pressure by water jets; circumferential surface fractures, subsurface flow and fracture, large scale plastic deformation leading to permanent deformation, shear deformation around the periphery of the impact zone, and failure due to reflection of stress waves.

In general the fractures observed in Missouri red granite were composites of all these types. Attempts were made to observe the development of fractures in the target by the jet (Figure 10). The impact of the jet formed a luminous ionized zone (Figure 14) which obscured both the jet and the target at the point of impact. No fractures in the targets were visible up to 52 microseconds after initiation. The fractures described below were developed due to the pressure exerted by the jet on the rock. The major fractures propagate in a radial manner from the hole suggesting failure due to tension. Also, fracturing continued beyond the jet termination point in concrete blocks.
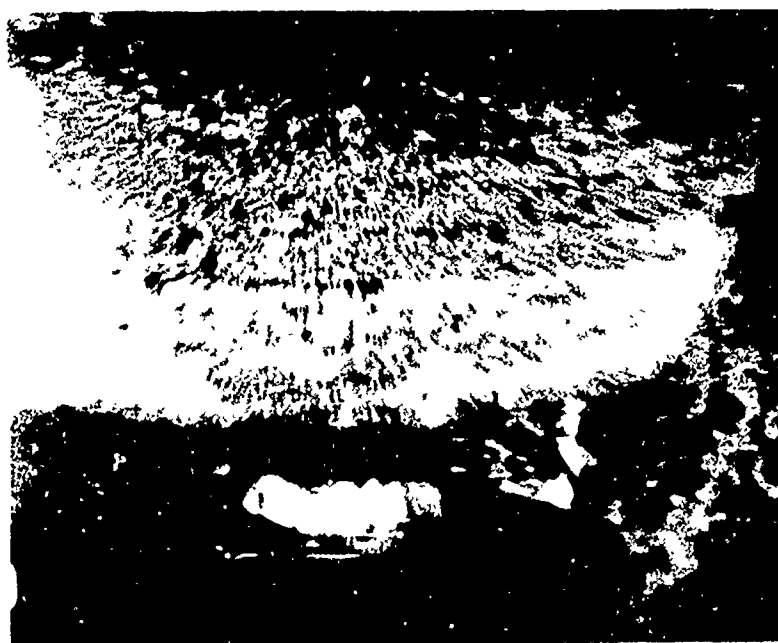
Figure 14. Detonation front and associated shock wave
52 μ sec after initiation

33

The pressure at the jet impact point is estimated to be on the order of 1.5×10^6 psi, and diminishes to about one-tenth this value at minimum penetration velocity. Thus, the duration of pressure at any one point along the axis of penetration is very short. A large portion of the energy is utilized in pulverizing the rock, plaster flow and in transmitting kinetic energy to the ejecta. It is estimated that less than three percent of the kinetic energy of the jet is finally converted to elastic wave energy in the rock. The outgoing wave from the jet hole was strong enough in many cases to cause radial fracturing (Figure 15). Concrete targets (Figure 16) also exhibited fracturing beyond the bottom of the jet hole, although some of the fractures may have been caused by waves reflected from the surface of the block. The rapid decrease in pressure effects outward from the axis of the hole is evident in Figure 17, which shows a zone of pulverization, grading into a zone where the crystals are fractured, and further where the minerals show little microfracturing.

Figure 15. Fracture pattern in granite
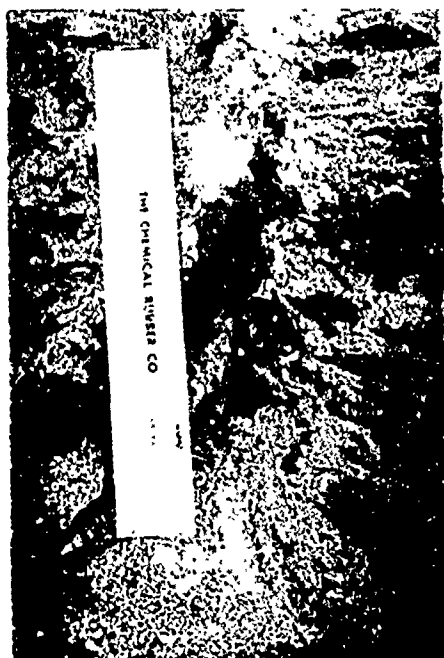
Figure 16. Longitudinal section of the shaped charge hole

D. Slug Formation and Metallographic Observations: As the liner begins to collapse due to the detonation pressure (Figure 1) the inner wall of the liner moves toward the cone axis at a greater speed than the outer wall. This causes a flow of the liner mass leading to fast jet formation from the inner wall and slow jet or slug formation from the outer wall. The process of cone collapse was photographed utilizing a mirror with a framing camera. Figure 17 shows the interior of a cone reflected in a mirror with the conical grid, and the development of the flow of the metal. The wall of the liner collapses toward the cone axis forming a solid conical slug and a jet. However, the latter is not visible.

Figure 17. Cone Collapse in Advanced Stage

35

Slugs from yellow brass cones were smaller than those of other metals. No slugs were recovered from Aluminum 7075. A carefully designed experiment was designed to collect slugs from aluminum liners, and one was obtained for Aluminum 2011. It is suggested that zinc in the alloy is responsible for small slugs, or for the lack of slug formation. Metallography studies were performed on the slugs and metals used for this investigation (Appendix C). The following conclusions were drawn from studies of the metallographs:

1) In all cases the grains have elongated and are oriented along the direction of the slug's longitudinal axis.

2) The grains in the slug are smaller than those in the metal. In all cases the size of the grains had reduced at least by a factor of ten.

3) The grain size is smallest near the axis of the slug and increases toward the edge.

4) In all of the slugs a pin hole or fracture was observed along the longitudinal axis.

5) For copper and possibly aluminum some evidence of melting was present. Material from the bottom of the target hole was analyzed microscopically. This revealed spherical inclusions indicating possible melting of copper particles (Figure 18)

6) There was indication of recrystallization and twinning in minerals in the granite.

7) The hardness of the slugs of aluminum 2011 and brass was less than the undeformed metal, suggesting an annealing effect. In monel and steel the hardness increased, suggesting a small degree of precipitation. However, no evidence of the precipitation was visible in the photomicrographs.

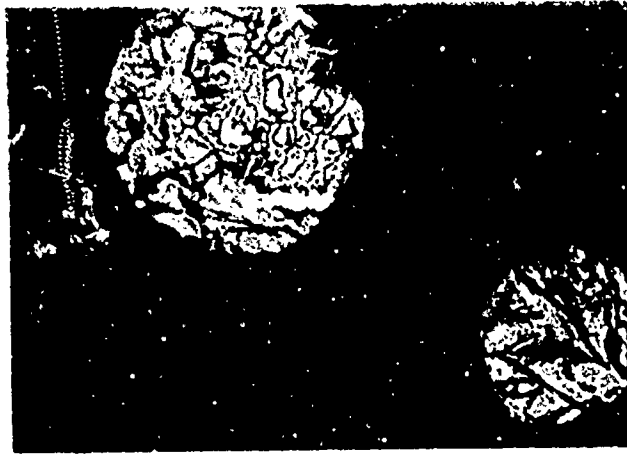8) There was no significant change in the densities of the metal in formation.

36

Figure 18. Photomicrograph of Copper imbedded in granite

x250

E. Jet Hole Characteristics: A great deal of comminuation took place in the material immediately around the hole where the work was crushed and friable. Spallation always occurred around the collar of the hole, probably due to rebound. Figure 19 shows the highly fractured granite with metal inclusions.
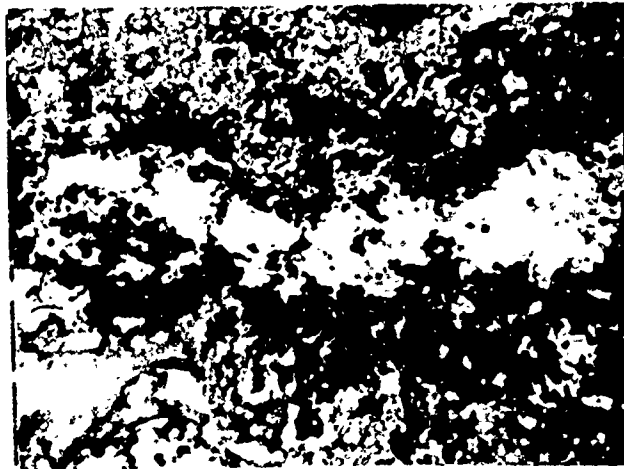

Figure 19. Photomicrograph of steel inclusion of inner wall of a hole in the granite

x250

37

All of the holes were coated with jet material, each having a coloration depending upon the liner metal. In the case of brass the holes were brick red while for copper the holes were red. Aluminum, monel, and steel gave a black coloration.

In all cases metal from the jet was deposited at the bottom of the holes in a fan shape. Four types of craters were formed (Figure 20). Type (d) had very smooth walls and they were discolored also by carbon from the explosive. As indicated above, some of the holes contained spherical globules indicating melting. However, except for one case (Figure 18) melting was not evidenced by optical microscopy. In some instances there was evidence of jet material intruding into the rock.

SUMMARY, CONCLUSIONS, AND RECOMMENDATIONS

1. Jets from the 60 degree monel, brass, and steel liners gave the deepest penetration. Monel required greater standoff than brass and steel, but less than aluminum.

2. Copper and brass liners gave equal penetration for 42 degree apex angles.

3. Aluminum liners were easier to machine than other metals. Maraging steel and the monel liners were the most difficult to fabricate.

4. Except for aluminum 7075 it appears that annealing has no effect on penetration in granite.

5. Aluminum 7075 jets gave a somewhat greater penetration than aluminum 2011.

6. Liners containing zinc produced small slugs or none at all.

7. The holes in the granite were uniform and approximated right circular cones. About 3 to 4 cm of the hole was removed by spalling and blast effects for 1½ in. diameter charges.

8. Fractures in granite due to the jet and blast were caused by compression, tension, and shear failure. Rock in the direct line of the jet was highly crushed and powdered, and the jet material had intruded into fractures in the rock.

9. Framing camera photography was inadequate to define jet characteristics in air although in an inert atmosphere it was possible to observe the jet for a few microseconds. Metallic probes (switches) were used to obtain jet tip velocity and rate of penetration into granite slabs using a pin oscilloscope technique.

10. Metallographic studies indicated a symmetrical liner collapse. Grains were highly fractured and hardness decreased in brass and aluminum, and
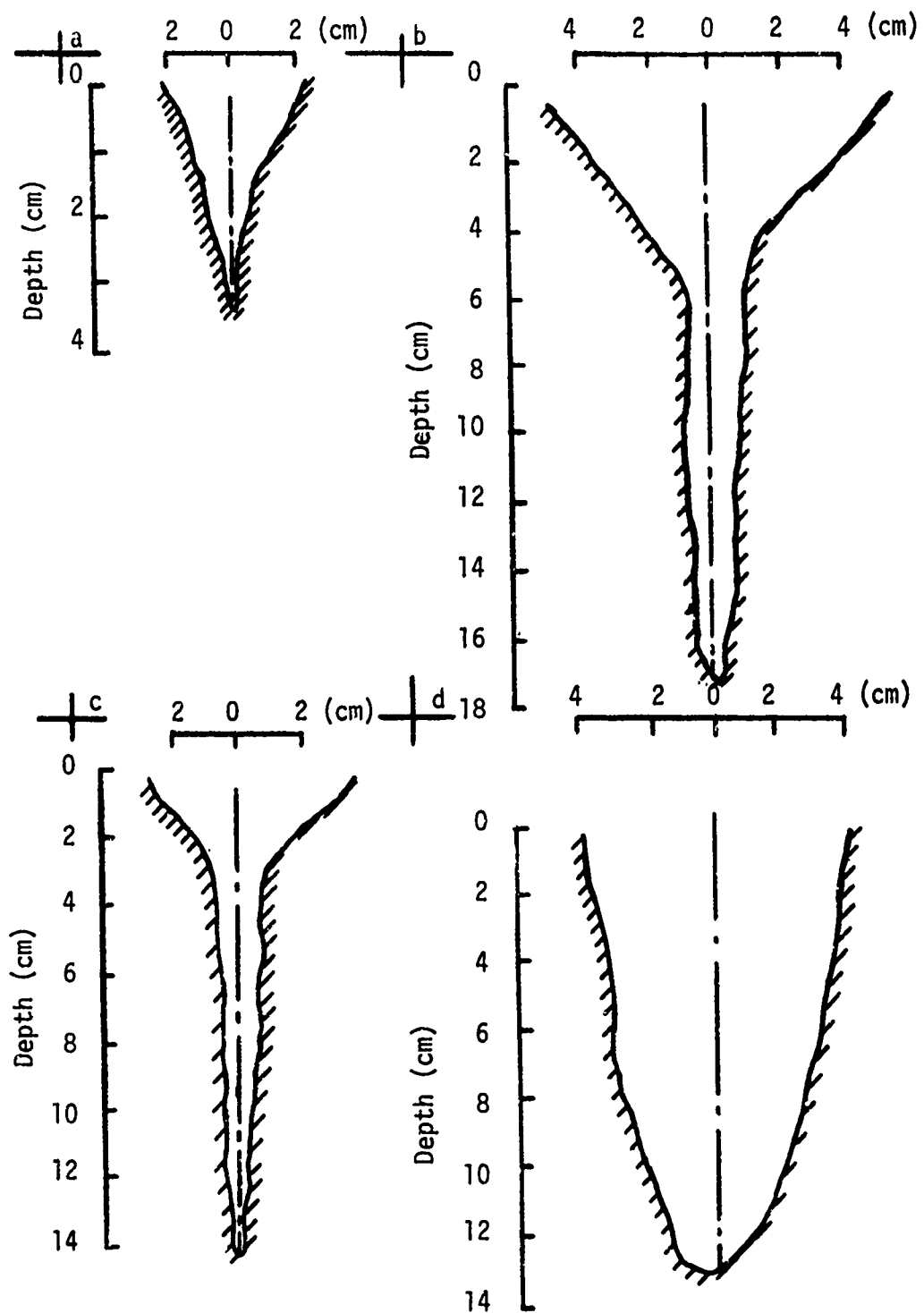
Figure 20. Typical hole profiles in granite

a phase transition was suspected in steel liners. The density of the slugs was the same as the undeformed metal.

11. A three-dimensional expression (Equation 3) was developed to describe the collapse time for conical liners. For an assumed constant collapse velocity the calculated stagnation point velocity was approximately constant.

12. Penetration parameters for granite could not be calculated from equations 4-7 due to inadequate information about the jet characteristics.

Recommendations:

1. An investigation should be carried out to obtain the jet characteristics and the minimum penetration velocities for different rocks. This information may be used to modify equations 4 through 7.

2. The three-dimensional theory should be verified using flash x-ray equipment.

3. With equations 4-7 and the three-dimensional collapse theory a computer program may be developed to evaluate shaped charge performance of different liners in rocks.

4. A more detailed metallurgical investigation should be undertaken to determine the behavior of metal liners under high pressures.

5. Studies should be continued to find liners which are more effective in penetrating rock. More effective explosives, geometries and other charge parameters are needed.

APPENDIX A

List of Symbols

CR	Cone radius
CD	Cone diameter
d	Wall thickness of cone
h	Height of the cone
H_{lim}	Limiting value of charge length
H.V.	Hole volume
L	Length of the jet
m	Mass per unit length
m_e	Mass of the liner element
P	Penetration
P_T	Total penetration
P_{max}	Maximum penetration
r_j	Radius of the jet
S	A point between S_2 and S_3
S_2	Normal distance to axis from inner wall of cone
S_3	Normal distance to axis from outer wall of cone
$\dot{S}$	Initial collapse velocity
S_{3i}	Initial value of S_3
SO	Stand off
T	Kinetic energy of collapse
t_1	Jet breakup time
t_c	Collapse time of liner
U_D	Detonation velocity of explosive

U^{min}	Minimum penetration velocity of target
V_j	Jet velocity
V_c	Collapse velocity of liner
V_j^o	Jet tip velocity
Z_o	Distance from virtual origin (assumed point of origin of jet) to the target surface
α	Half apex angle
β	Collapse angle
γ	$\sqrt{\rho_t / \rho_j}$
Δl	Length of element along the slant height of cone
λ	Correction factor for discontinuous jet
ρ_t	Density of target
ρ_j	Density of jet

APPENDIX B

Collapse Time and Kinetic Energy

The following assumptions were used in the development of the expressions presented in the text to obtain liner collapse time and the kinetic energy of collapse:

1. Metal under high pressure and impulsive load is considered to be an incompressible fluid.
2. Collapse is normal to the original slant height of the cone.
3. The initial collapse velocity is constant over the surface of the cone.

Consider a section of the cone and an element on the surface having a small length along the slant height of the cone to be $\Delta\ell$ (Figure 2). Thus,

$$r_2 = S_2 \, \text{Cos} \, \alpha$$

$$r_3 = S_3 \, \text{Cos} \, \alpha$$

and the volume of this element

$$V_e = \tfrac{1}{2}\Delta\ell \rho \pi \text{Cos} \, (S_2^2 - S_3^2) \qquad (1)$$

If the volume of the element remains constant then

$$V_e = \text{constant}$$

and therefore

$$(2V_e / \pi \text{Cos} \alpha \Delta\ell) = (S_2^2 - S_3^2)$$

will be conserved as the liner is collapsing. Differentiating $(S_2^2 - S_3^2)$ with respect to time

$$2S_2 \dot{S}_2 = 2S_3 \dot{S}_3 = 2S\dot{S}$$

for any value of S, thus

$$\dot{S}_3 = (S \, \dot{S} \, / \, S_3) \qquad (2)$$

43

The kinetic energy (T) of the element is given by

$$T = \tfrac{1}{2}\Delta\ell\rho \int_0^{2\pi\cos\alpha} \int_{S_3}^{S_2} dAS \; dS \; (dS/dt)^2$$

$$= \Delta\ell\rho\pi\cos\alpha \int_{S_3}^{S_2} S \; (S \; dS/dt)^2 \; 1/(S^2) \; dS$$

$$= \Delta\ell\rho\pi\cos\alpha \; (S_3\dot{S}_3)^2 \int_{S_3}^{S_2} (1/S) \; dS$$

$$T = \Delta\ell\rho\pi\cos\alpha \; (S_3 \; \dot{S}_3)^2 \; \ln(S_2/S_3) \qquad (3)$$

From Equation (3) $\dot{S}_3$ is given by

$$\left[dS_3/dt\right]^2 = \left(\dot{S}_3\right)^2 = \left[\frac{T}{\Delta\ell\rho\pi\cos\alpha S_3^2 \; \ln \; S_2/S_3}\right]$$

Therefore

$$dt = \left[\frac{\Delta\ell\rho\pi\cos\alpha S_3^2 \; \ln \; S_2/S_3}{T}\right]^{\tfrac{1}{2}} dS_3 \qquad (4)$$

Integrating Equation (4) for t gives

$$\int_0^t dt = (\rho\pi\Delta\ell\cos\alpha/T)^{\tfrac{1}{2}} \int_{r_j}^{S_{3i}} S_3 \; (\ln \; S_2/S_3)^{\tfrac{1}{2}} \; dS_3$$

Therefore

$$t_c = (\rho\pi\Delta\ell\cos\alpha/T)^{\tfrac{1}{2}} \; 1/2 \int_{r_j/\cos\alpha}^{S_{3i}} S_3 \ln\left(\frac{S_3 + d}{S_3}\right) dS_3$$

44

APPENDIX C

Metallography of the Metals and Slugs

The changes in microstructure following explosive impact and flow are primarily in the distribution density of lattice defects such as dislocations, vacancies, interstitials, stacking faults, mechanical twins, and an amount of strain induced transformation in alloys normally susceptible to such transitions (26). The large amount of energy imparted to the liners by explosives causes a severe deformation and reduction in size of the grains. A systematic metallographic investigation was made to observe the effect of high pressure generated by Composition C-4 on the liners.

A representative sample was taken from each of the metals used to fabricate the cones. Samples were prepared for metallographic analysis employing standard procedures (27).

The slugs were cut and mounted in a manner to reveal the structure along the longitudinal as well as the transverse axis. The greatest deformation was near the center of the slug. The grains showed a flow in the direction of the metal toward the stagnation point. In some cases fracture at the stagnation zone was observed. Metallographs are presented in Figures 1C-16C.

Figure 1C: Metallograph of aluminum 2011 (T-3). This alloy has a face centered cubic lattice structure. It is a free machining alloy. Grain boundaries are well defined and are equiaxed.

Figure 2C: Metallograph of aluminum 2011 slug. The grains are highly fractured and are about 1/150th of the original grain size. Some recrystallization is indicated. Fine grains are almost equiaxed. A fracture was seen along the transverse axis of the slug near the stagnation axis. The hardness of the metal had decreased from 63 RB to 21 RB.

Figure 3C: Metallograph of aluminum 7075 (T-6). This is an aluminum zinc alloy. No slug was recovered in this case. The α grains are well defined and are equiaxed. Mostly α grains with some black inclusions and boundary precipitation can be seen.

Figure 4C: Metallograph of yellow brass. The α grains are white and occupy about 90 percent of the area of the specimen. The grains are well defined and are equiaxed.

Figure 5C: Metallograph of the brass slug taken along the longitudinal axis near the edge of the slug. The grains are fractured and

45

show elongation along the slug axis. The β particles had elongated near the center of the slug and were highly fractured. The flow of the particles was along the transverse axis of the slug. The hardness had decreased from 73 RB to 53 RB suggesting some annealing effects.

Figures 6C, 7C and 19: Metallographs of the copper metal, slug, and a photomicrograph of a copper particle imbedded in granite. In Figure 6C annealing twins are visible. The grains are well defined and are equiaxed. Figure 7C shows the structure of the slug along the longitudinal axis of the slug. No fractures were visible but a pin hole was observed at the center of the slug. The grains are well defined and are equiaxed. The size of the grains is about 1/10th of the original grains. Grains are elongated along the direction of flow. No melting was observed. The grains are completely crushed. Recrystallization after deformation is apparent. Figure 19 is a photomicrograph of the metal particles and highly fractured granite from the end of the hole. Some melting of the metal is evidenced. The hardness of the slug had increased from 34 RE to 14.5 RB.

Figure 8C: Metallograph of monel which shows a roughly equiaxed grain of β phase containing annealing twins and no second phase. Small amounts of an unidentified second phase inclusion are seen.

Figures 9C, 10C, and 11C: Figure 9C is a metallograph of a monel slug taken along the longitudinal axis. The grains are highly deformed and have elongated along the direction of flow. Heavy deformations and flow patterns are clearly visible. Black inclusions of a second phase are lenticular in shape. Figure 10C shows the structure of the slug at the center. The stagnation point has a large crack and small fractures in a radial pattern. Figure 11C shows the crack at the center surrounded by very fine recrystallized grains, several orders of magnitude smaller than the original grains, gradiating up to 10 percent of the original metal grains. The hardness of the slug had increased from 12.5 RC to 21 RC.

Figures 12C and 13C: Metallographs of maraging steel (Vascomax 250). The grain boundaries are well defined and the grains are equiaxed. Annealing twins are visible. Figure 13C was taken at the edge of the transverse axis of the slug. White lines are fractures while the black area is unidentified.

46

Figure 14C: A sketch of the steel slug showing variations in hardness. The outer edge of the metal was fractured. These fractured. These fractures extend toward the center in a conical pattern.

Figures 15C and 16C: Metallographs of the structure at the edge of the steel slug along the longitudinal axis and at the center of the slug. No microstructure is visible at this magnification. Some phase transformation is suspected. The grains increase in size away from the center. The hardness of the slug had increased from 28.5 RC to 36.75 RC (average), suggesting some degree of precipitation. It was not possible to see precipitates by optical microscopy.

Figure 1C.   Aluminum 2011

x250

NOT REPRODUCIBLE
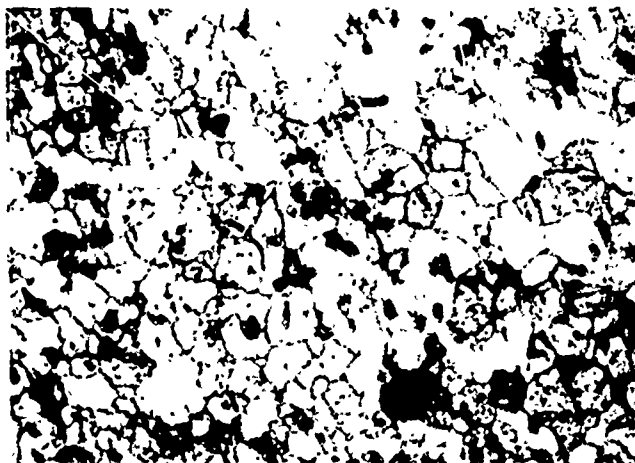
Figure 2C.   Aluminum 2011 Slug

x250
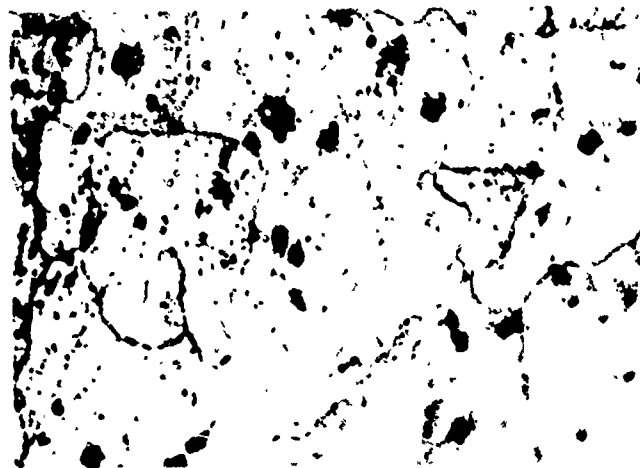
Figure 3C.   Aluminum 7075

x250

NOT REPRODUCIBLE
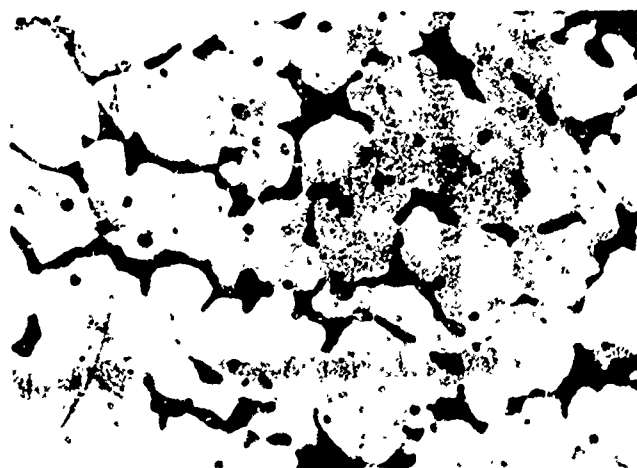
Figure 4C.   Yellow Brass

x250
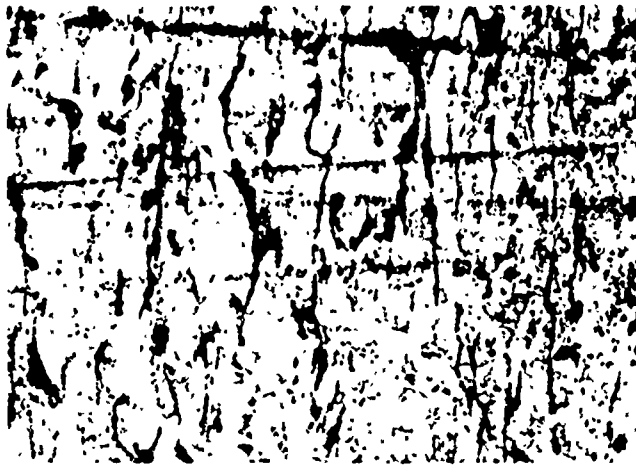
Figure 5C.   Side of slug, yellow brass

x250

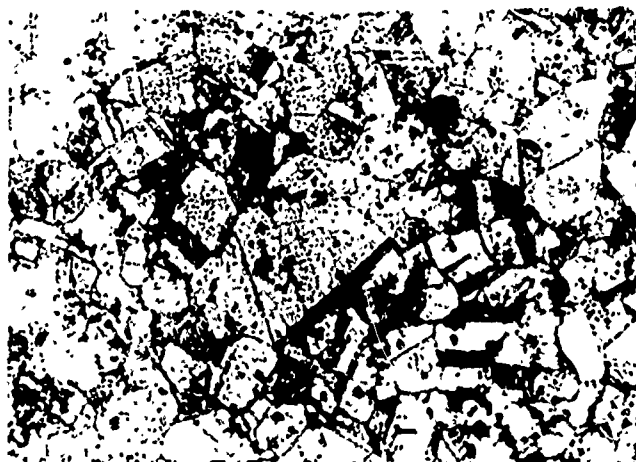NOT REPRODUCIBLE

Figure 6C.   Copper

x250

Figure 7C. Copper slug

x250

NOT REPRODUCIBLE

Figure 8C. Monel

x250

51

Figure 9C. Monel slug. Taken along the transverse axis.
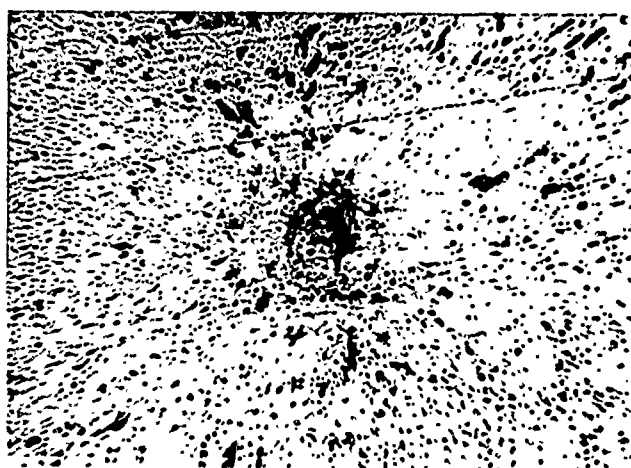
x250

NOT REPRODUCIBLE

Figure 10C. Center of the slug, Monel

x250

52

Figure 11C. Monel slug along transverse axis. Recrystallization near the center can be seen.

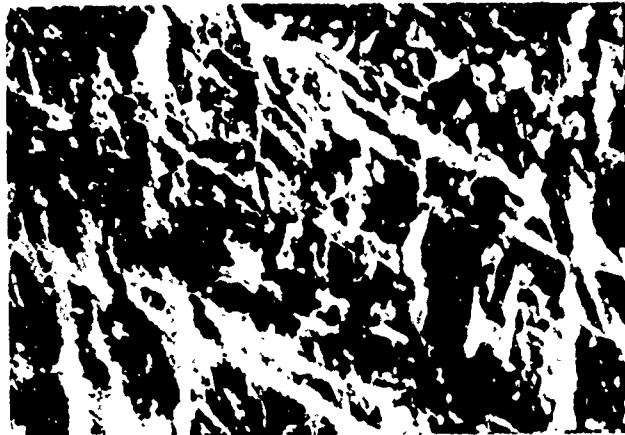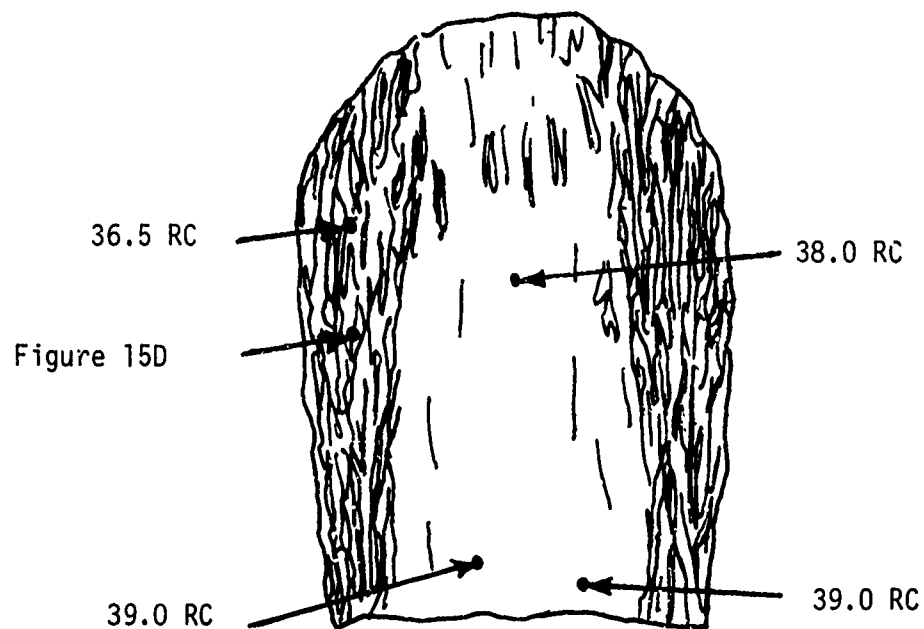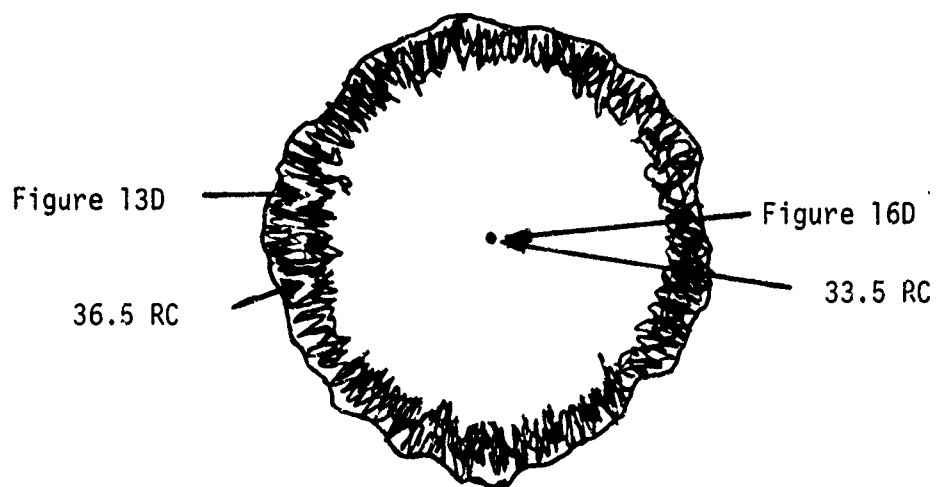x250

NOT REPRODUCIBLE

Figure 12C. Maraging

x250

53

Figure 13C. Steel slug

x250

36.5 RC

38.0 RC

Figure 15D

39.0 RC

39.0 RC

LONGITUDINAL SECTION

NOT REPRODUCIBLE

Figure 13D

Figure 16D

33.5 RC

36.5 RC

TRANSVERSE SECTION

Figure 14D. Steel Slug and Its Hardness
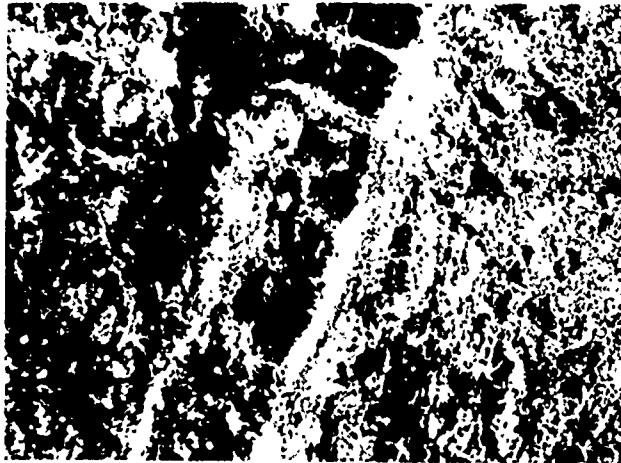
55

Figure 15C. Maraging steel slug at edge

x250

NOT REPRODUCIBLE

Figure 16C. Maraging steel slug at center

x250

56

REFERENCES

1. Birkhoff, G., MacDougal, D.P., Pugh, E.M., and Sir Taylor, G.,
   "Explosives with Lines Cavities", _Journal of Applied Physics_,
   (1948), Vol. 19, 563-582.

2. Baum, F.A., Stanykovich, R.P., and Shekter, B.I., _Physics of
   an Explosion_, (AD 400 151), New York, Research Information
   Service, (1949), 546.

3. Eichelberger, R.J., "Re-Examination of the Theories of Jet Forma-
   tion and Target Penetration by Lined Cavity Charges", Ph.D. disser-
   tation, Carnegie Institution of Technology, Pittsburgh, (1954).

4. Clark, G.B., "Studies of the Design of Shaped Charges and Their
   Effect in Breaking Concrete Blocks", _American Institute of Mining
   Engineers_, Technical Paper 2157, (1947).

5. Austin, F.C., "Lined-Cavity Charges and Their use in Rock and Earth
   Materials", _New Mexico Institute of Technology_, Bulletin 69, (1959).

6. Huttl, J.B., "The Shaped Charge for Cheaper Mine Blasting", _Engineer-
   ing and Mining Journal_, (1946), Vol. 147, 58-63.

7. Hill, R., MVtt, H.F., and Pack, D.C., "Penetration by Munroe Jets",
   Ministry of Supply, A.C. No. 5756, HMSO, London, January, (1944).

8. Pack, D.C., and Evans, W.M., "Penetration by High Velocity Munroe
   Jets-I", _Proceedings of the Physical Society of London_, (1951), Sec-
   tion B, Vol. 64, 298.

9. Pack, D.C., and Evans, W.M., "Penetration by High Velocity Munroe
   Jets-II", _Proceedings of the Physical Society of London_, (1951),
   Section B, Vol. 64, 303.

10. Pugh, E.M., Eichelberger, R.J., and Rostoker, N., "Theory of Jet
    Formation by Charges with Lined Conical Cavities", _Journal of Applied
    Physics_, (1952), Vol. 23, 532.

11. Sterne, T.E., "A Note on Collapsing Cylindrical Shells", _Journal of
    Applied Physics_, (1950), Vol. 21, 73-74.

12. Eichelberger, R.J., "Prediction of Shaped Charge Performance from
    Release Wave Theory", _Transactions of the Symposium on Shaped
    Charges, BRL 909 (AD 58 899)_, Aberdeen Proving Grounds Maryland,
    (1953), 192.

13. Jackson, R.F., "The Problem of Lagrange for Shaped Charge Liner
    Collapse", _Transactions of the Symposium on Shaped Charges,
    BRL 909 (AD 58 899)_, Aberdeen Proving Grounds, Maryland, (1952), 131.

14. Dipersio, R., Simon, J., and Merendino, A.B., "Penetration of Shaped
    Charge Jet into Metallic Targets", _BRL 1296 (AD 476 717)_, Aberdeen
    Proving Grounds, Maryland, (1965).

15. Allison, F.E., and Vitali, R., "A New Method of Computing Penetration Variables by Shaped Charge Jets", BRL 1184 (AD 400 485), Aberdeen Proving Grounds, Maryland, (1963).

16. Klamer, O.A., "Shaped Charge Scaling", AD 600 273, Picatinny Arsenal, Dover, New Jersey, (1964).

17. Zernow, L., and Simon, J., "High Strain Plasticity of Liner Metals and Jet Behavior", Transactions of the Symposium on Shaped Charges, BRL 909 (AD 58 899), Aberdeen Proving Grounds, Maryland, (1953), 107-130.

18. Rinehart, J.S., and Pearson, J., Behavior of Metals Under Impulsive Loads, New York, Dover Publications, (1965), 203.

19. Brimmer, R.A., "Manual for Shaped Charge Design", Navord Report 1248 (ATI 84 949), China Lake, California, (1950).

20. Winn, H., "The Present Status of the Artillery Ammunition Program at the Firestone Tire and Rubber Company", Transactions of the Symposium on Shaped Charges, BRL 909 (AD 58 899), Aberdeen Proving Grounds, Aberdeen, Maryland, (1953), 25.

21. Brown, J., Personal Communication.

22. Bowden, F.P., Brunton, J.H., "The Deformation of Solids by Liquid Impact at Supersonic Speeds", Proceedings of the Royal Society of London, (1961), Series A, Vol. 263, (1961), 433.

23. E.I. Dupont and Co., "Investigation of Cavity Effect", Final Report, E.I. Dupont De Nemours and Co., Wilmington, Delaware, (1943).

24. E.I. Dupont and Co., "Evaluation of Deep Drawing Steels for Manufacture of Purity Charge Cones", E.I. Dupont De Nemours and Co., Wilmington, Delaware, (1944).

25. Clark, J.C., "Flash Radiography Applied to Ordinance Problems", Journal of Applied Physics, (1949), Vol. 20, 363-370.

26. Orava, R.N., and Otto, H.E., "The Effect of High Energy Rate Forming on Terminal Characteristics of Metal-A Review", Journal of Metals, (February 1970), 17-30.

27. Kehl, G.H., Principles of Metallographic Laboratory Practice, 3rd Edition, New York, McGraw-Hill Co., (1944).